

---

# HOMOGENEOUS NUCLEATION OF SHEARED LIQUIDS: ADVANCES AND INSIGHTS FROM SIMULATIONS AND THEORY

---

A PREPRINT

 **Amrita Goswami**

Department of Chemical Engineering  
Indian Institute of Technology Kanpur  
amritag@iitk.ac.in

 **Jayant K. Singh\***

Department of Chemical Engineering  
Indian Institute of Technology Kanpur  
jayantks@iitk.ac.in

June 29, 2021

## ABSTRACT

One of the most ubiquitous and technologically important phenomena in nature is the nucleation of homogeneous flowing systems. The microscopic effects of shear on a nucleating system are still imperfectly understood, although in recent years a consistent picture has emerged. The opposing effects of shear can be split into two major contributions for simple liquids: increase of the energetic cost of nucleation, and enhancement of the kinetics. In this review, we describe the latest computational and theoretical techniques which have been developed over the past two decades. We collate and unify the overarching influences of shear, temperature, and supersaturation on the process of homogeneous nucleation. Experimental techniques and capabilities are discussed, against the backdrop of results from simulations and theory. Although we primarily focus on simple liquids, we also touch upon the sheared nucleation of more complex systems, including glasses and polymer melts. We speculate on the promising directions and possible advances that could come to fruition in the future.

**Keywords** rare-event, nucleation, shear, seeding, Classical Nucleation Theory

## 1 Introduction

Understanding quiescent homogeneous nucleation has been a longstanding goal of the academic community, which is justifiable considering its immense importance in various scientific and industrial applications [1–7]. Quiescent homogeneous nucleation is opaque to interpretations across the spectrum of modern techniques, from both theoretical and experimental viewpoints. The process of quiescent homogeneous nucleation is notoriously challenging to study using computational methods, since it is a stochastic rare event in terms of the time and length scales. On the other side of the spectrum, nucleation experiments are plagued by rapid crystallization or vitrification [8] which can be difficult to capture microscopically [9]. A phenomenon of perhaps even greater theoretical and technological relevance [10–14] is the nucleation of flowing liquids—in reality, liquids are rarely static.

The existing literature is somewhat divided on the topic of the effect of shear and its influence on nucleation. Certain results indicate that shear impedes and inhibits nucleation [15, 16], while others suggest that flow induces or enhances nucleation [17–23]. These seemingly conflicting results can be reconciled within a broader context, bolstered by experimental [24, 25] and computational [26–36] studies which imply that the nucleation rate is non-monotonic with shear. A linear flow field tends to deform incipient clusters. This shear deformation affects the energetics of the nucleation process. At the same time, an imposed shear rate encourages the diffusive motion of the particles in a simple liquid, tending to enhance the kinetics of nucleation. The ordering of polymer strands can also be facilitated by shear. A detailed and unified evaluation of these underlying mechanisms forms the kernel of this review.

The study of sheared homogeneous nucleation, particularly of simple liquids, glassy systems and colloids, via theory and simulations is a burgeoning field. Theoretical and simulation studies of sheared nucleation have experienced something of a renaissance in the past decade, partly due to the surge in computational power [37]. We elucidate recent theoretical developments and advances in the field, focusing mostly on simple liquids. This paper is organized as follows: in

the remaining introductory sections, we provide a brief overview of Classical Nucleation Theory (Section 1.1) and the seeding method (Section 1.2) for quiescent homogeneous nucleation. Section 2 is dedicated to computational strategies which can be used for sheared homogeneous nucleation, describing brute-force approaches (Section 2.1), forward-flux sampling (Section 2.2), and recent CNT-based approaches (Section 2.3). In Section 3 we expound the various effects of shear on homogeneous nucleation behaviour obtained from simulations and theory, and explore microscopic mechanisms. Section 3.6 covers experiments, emphasizing current capabilities of typical experimental techniques. Finally, in Section 3.7, we summarize the major conclusions, highlight exciting possible extensions of the field, and identify future challenges.

## 1.1 Overview of Conventional CNT

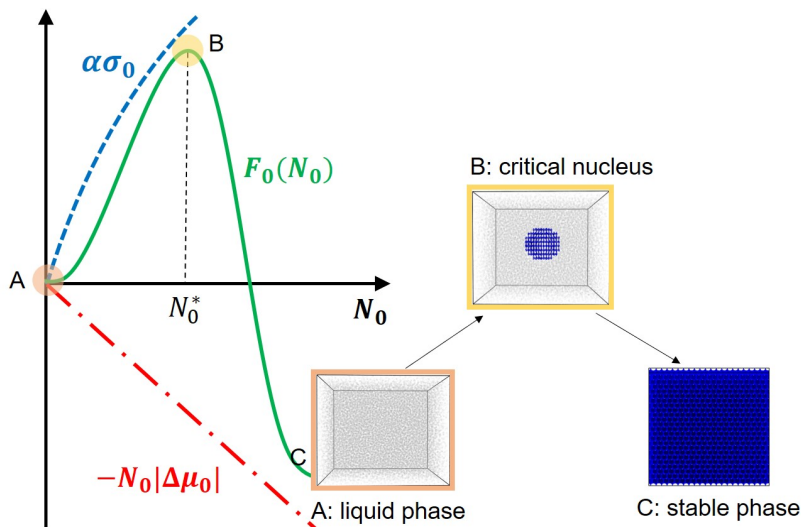


Figure 1: Schematic of the free energy curve for homogeneous nucleation,  $F_0(N_0)$ . The favourable volume contribution to the free energy,  $\alpha\sigma_0$ , and unfavourable interfacial free energy cost,  $-N_0|\Delta\mu_0|$ , are indicated with blue and red dashed lines, respectively. Insets depict various theoretical stages of the nucleation process, from the initial state (A) to the final stable phase (C).

Classical Nucleation Theory (CNT) is an approximate phenomenological theory, whose ubiquity cannot be overstated even though about 100 years have passed since its conception. Aspects of CNT are ingrained some form in virtually every computer simulation of homogeneous nucleation of simple liquids. Exhaustive treatments and reviews of CNT are available elsewhere in the literature [2, 38–40]. Here, we summarize details of relevance for further extensions to sheared homogeneous nucleation.

Originally formulated for describing the condensation of a vapour into a liquid, CNT has since been found to be applicable to other phase transitions. In particular, extensions to CNT have dominated descriptions of crystal nucleation of supercooled and supersaturated solutions. The cornerstone of CNT is the assumption that microscopic crystalline nuclei can be effectively treated as scaled-down replicas of the macroscopic crystalline phase. These crystalline clusters are considered to be separated from the metastable phase by a "dividing surface" of negligible thickness. This negligibly thin and sharp "dividing surface" is a convenient construct and not a statement about the molecules and their physical reality. Furthermore, CNT assumes that crystal nucleation is a single-step process, wherein the only significant barrier is the free energy barrier arising from the interplay of the solid-liquid interfacial energy,  $\sigma_0$ , and the chemical potential difference,  $\Delta\mu_0$ . All other contributions to the free energy are neglected.

With these assumptions, in the archetypal CNT formulation, the free energy of formation  $F_0$  of a spherical crystallite nucleus, containing  $N_0$  particles, is expressed as the sum of a favourable volume term and an unfavourable surface term [9, 38, 41–43]:

$$F_0(N_0) = \underbrace{-N_0|\Delta\mu_0|}_{\text{volume term}} + \underbrace{\alpha\sigma_0}_{\text{surface term}}, \quad (1)$$

where  $\Delta\mu_0$  is the chemical potential difference between the metastable liquid phase and the crystal,  $\sigma_0$  is the crystal-fluid interfacial free energy,  $\alpha = (36\pi N_0^2 v'^2)^{\frac{1}{3}}$  is the geometric shape factor of a spherical nucleus, and  $v'$  is the volume of one unit particle or molecule in the crystal. In order to emphasize the fact that quintessential CNT is used for quiescent systems not under the influence of shear, the subscript 0 has been used for the concerned variables. For example, the system is assumed to be quiescent in the calculation of the quantities  $F_0$ ,  $N_0$ ,  $\Delta\mu_0$  and  $\sigma_0$  in Eq. (1). This convention will be adopted throughout this review to refer to parameters that are estimated in the absence of flow.

In Eq. (1),  $N_0|\Delta\mu_0|$  is the driving force for the nucleation process, arising from the greater thermodynamic stability of the solid phase, compared to the metastable liquid phase [38, 44]. The free energy cost of forming the hypothetical interface is given by  $\alpha\sigma_0$ . The competition between the favourable and unfavourable terms yields a maximum in  $F_0(N_0)$ , indicative of a kinetic barrier to the phase transformation, depicted in Figure 1.

Crystalline clusters form spontaneously via stochastic, localized fluctuations. A physical interpretation of Eq. (1) is that the unfavourable surface term dominates for small nuclei, which consequently tend to dissipate into the liquid phase unless they are aided by fortuitous fluctuations. A cluster grows spontaneously, overcoming the free energy barrier, only if it exceeds a critical size [45]. The CNT expression for this free energy barrier for nucleation is given by:

$$F_0(N_0^*) = \frac{N_0^*|\Delta\mu_0|}{2} = \frac{16\pi v'^2 \sigma_0^3}{3|\Delta\mu_0|^2}, \quad (2)$$

where  $F_0(N_0^*)$  is the height of the free energy barrier, and  $N_0^*$  is the number of particles or molecules in the critical cluster. Thus, the stochastic regime, preceding the formation of the critical nucleus, gives way to crystal growth, which is a deterministic thermodynamically driven regime.

Assuming that crystalline nuclei grow or shrink due to the attachment or dissolution of atoms (or ‘monomers’) one-by-one the steady-state rate of nucleation can be estimated from an Arrhenius reaction rate type equation: [38, 46–48]

$$J_0 = \rho_l Z_0 f_0^+ e^{-\frac{F_0(N_0^*)}{k_B T}}, \quad (3)$$

where  $\rho_l$  is the number density of the supercooled liquid,  $Z_0$  is the Zeldovich factor [38], and  $f_0^+$  is the rate of attachment of molecules to the cluster in units of inverse time.  $k_B$  is the Boltzmann constant, and  $T$  is the temperature. The Zeldovich factor,  $Z_0$ , captures the multiple possible re-crossings of the free energy barrier [49] and is related to the curvature of the free energy curve at the critical cluster size  $N_0^*$ .

The nucleation rate is thus proportional to the thermodynamic probability of a fluctuation yielding the formation of a critical cluster, and a dynamical factor ( $\rho_l Z_0 f_0^+$ ), called the kinetic prefactor. Since  $f_0^+$  is related to the time required for a single particle or molecule to attach itself to the solid cluster, it can be expressed as [38, 46]:

$$f_0^+ = \frac{24D_0(N_0^*)^{\frac{2}{3}}}{\lambda^2}, \quad (4)$$

where  $D_0$  is the bulk self-diffusion coefficient of the supercooled liquid phase at a particular temperature  $T$ ,  $\lambda$  is the atomic ‘jump length’, estimated to be about one molecule diameter.

Therefore, CNT provides a convenient theoretical framework for calculating the free energies (Eq. 2) and nucleation rates (Eq. 3). However, CNT involves several simplifying assumptions, which we enumerate and summarize briefly, revealing the shortcomings of the theory.

1. Conventional CNT assumes that nucleation proceeds according to a single-step mechanism, via which clusters of the ordered phase form directly from the metastable parent phase. However, there is considerable theoretical and experimental evidence for a two-step model of nucleation for proteins [50–57] and supersaturated solutions [58–64], which asserts that a cluster of monomers forms first, followed by reorganization into the ordered phase, i.e., the cluster size and order parameter are decoupled. Meticulous reviews in the literature have covered two-step and non-classical nucleation in detail [65–75]. In this review, we focus on single-component systems which can be reasonably presumed to follow a single-step mechanism.
2. The slow kinetics originate solely from the free energy barrier, and microscopic motions are fast compared to the time-scales of nucleation. In other words, only the slower degrees of freedom contribute to the free energy barrier. The size of the crystal embryo changes via the attachment or detachment of monomers one at a time [69]. Where the microscopic motions show a tendency towards colloidal aggregation or secondary structure,

the CNT model fails. In particular, conventional CNT typically cannot be applied without further extensions to glassy liquids and polymer systems, which are prone to ageing and ‘slow’ rearrangement of molecules or chains [76, 77].

3. In quintessential CNT, the nucleus is assumed to be perfectly spherical. This has been shown to be a reasonable approximation for water [78, 79]. CNT has also been extended for ellipsoidal clusters [80].
4. The embryos are assumed to be perfectly identical to the bulk ice phase, and are thus conceptualized as fragments of the bulk phase. Finite size effects on the physical and structural properties of the nuclei are wholly neglected.
5. The solid-liquid interface is considered to be a sharp dividing surface. However, in reality, the interfacial region is finite, and tends to be a few molecules thick. This approximation is more glaringly inaccurate for smaller nuclei wherein the interfacial molecules form a significant proportion.
6. The microscopic description of the interfacial energy  $\sigma_0$ , is only theoretically defined for a hypothetical isotropic nucleus (an assumption which often falls under the purview of the ideal ‘capillary approximation’), and can be ambiguous for real systems [40, 44]. In early CNT formulations, the solid-liquid interfacial energy,  $\sigma_0$ , at any temperature was assumed to be constant and equal to the macroscopic interfacial energy at the equilibrium freezing temperature [39]. This approximation presumes that neither the curvature of nucleus nor the temperature has an effect on  $\sigma_0$ . However, subsequent extensions to CNT account for the effect of the nucleus size, curvature and supercooling in the estimation of  $\sigma_0$ . These modified CNT-based techniques include the so-called ‘seeding method’ [81–83] and a formulation invoking additional corrections for fuzzy solid-liquid interfaces and non-spherical cluster shapes [84]. We elaborate the seeding class of techniques in this review, and demonstrate how they can be employed for sheared liquids.

Despite these inherent caveats, CNT has been shown to be surprisingly accurate [81], and is often the pragmatic technique of choice due to its simplicity and wide applicability. CNT results are also used as a benchmark for comparing and discussing qualitative trends with more sophisticated approaches [85, 86]. In the remaining sections, we show that CNT provides a convenient basis for describing the nucleation of sheared supercooled liquids. Nevertheless, the gross simplifying assumptions make CNT far from a universal panacea.

## 1.2 CNT and the Seeding Method

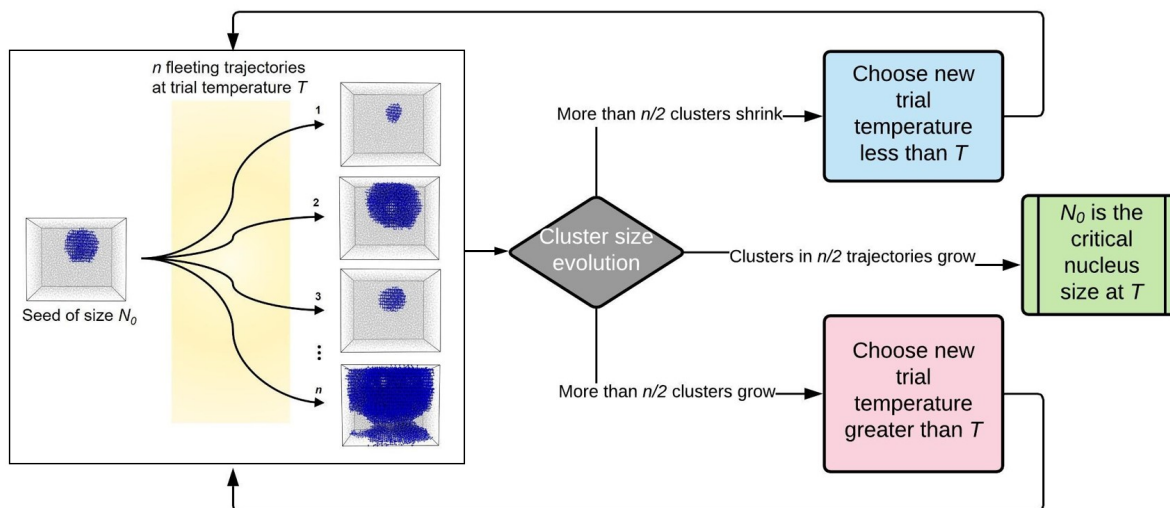


Figure 2: Flow chart of a typical implementation of the seeding technique. The inserted seed size,  $N_0$ , is known. Collections of  $n$  trajectories are run at trial temperatures iteratively, until a temperature is found at which clusters in about  $n/2$  trajectories enlarge, while those in the remaining  $n/2$  trajectories decrease in size. Alternatively, if the critical nucleus size at a specific value of  $T$  is desired, the seed size,  $N_0$ , is iteratively modified until the stopping criterion is satisfied.

Perhaps the most egregious of the CNT assumptions is the capillary approximation. Elements of this approximation can be dismantled by estimating the interfacial energy,  $\sigma_0$ , as a function of the critical cluster curvature and supercooling. A popular technique for such calculations of  $\sigma_0$  is the seeding method, which is an approximate simulation approach used within the framework of CNT [81–83].

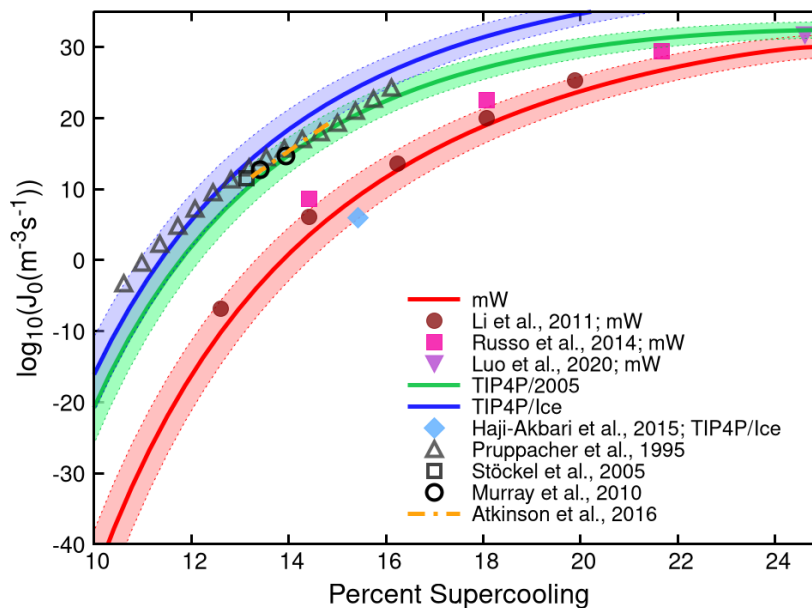


Figure 3: Comparison of the homogeneous nucleation rates,  $J_0$ , as a function of the percent supercooling, estimated using the seeding method (solid lines) for the mW, TIP4P/2005 and TIP4P/Ice water models, with results obtained from experiments (open symbols and dashed line) and other simulation strategies (filled symbols). The shaded regions flanking the solid lines denote the errors associated with seeding calculations [78].  $J_0$  was calculated via seeding, using data from Espinosa et al. [78] and power law fits to the diffusion coefficients. Results for the mW model are denoted by filled maroon circles, magenta squares, and an inverted mauve triangle, obtained via FFS calculations by Li et al. [87], a modified umbrella sampling scheme by Russo et al. [88], and MFPT calculations by Luo et al. [34], respectively. The filled blue diamond represents the rate for the TIP4P/Ice model estimated via FFS, at 230 K by Haji-Akbari et al [85]. Experimental rate estimates were reported by Pruppacher et al [89]. (open grey triangles), Stöckel et al [90]. (open grey squares), Murray et al [91]. (open black circles), and Atkinson et al [92] (mustard dashed line).

The seeding method, which was first proposed by Bai et al [81, 93], can reliably determine details of the critical nucleus, at a particular condition of metastability. When used in tandem with CNT, the seeding technique is capable of estimating interfacial free energies from microscopic data, along with the free energies and rates for conditions of shallow metastability, which are generally inaccessible to brute-force approaches [78, 79, 82, 83, 94–96].

In the seeding technique [81, 93], the critical nucleus size  $N_0^*$  is determined at a particular temperature, using seeded MD (Molecular Dynamics) simulations. Figure 2 outlines the procedure of the seeding technique. A solid spherical cluster of the stable crystal phase (or ‘seed’) is artificially inserted into supercooled liquid configurations. The seed dimensions are chosen prior to insertion. The evolution of cluster sizes of the largest clusters, in a swarm of independent fleeting trajectories, is then monitored at predetermined trial temperatures. The temperature at which the ‘largest’ clusters (determined using an appropriate order parameter) grow in roughly half of the trajectories is the temperature at which the inserted initial cluster size ( $N_0$  in Figure 2) is critical ( that is,  $N_0 = N_0^*$  at  $T$ ). This scenario corresponds to the top of the free energy barrier, where a particular cluster of the ordered phase, with  $N_0^*$  particles, may either re-disperse into the liquid phase or increase in size. Therefore, using seeded simulations, the value of  $N_0^*$  is fixed at a particular temperature  $T$ .

The estimated  $N_0^*$  is subsequently used to obtain  $\sigma_0$ , assuming that the free-energy profile obeys CNT. Now the interfacial energy  $\sigma_0$ , can be determined according to the relation

$$\sigma_0 = \left( \frac{3N_0^*}{32\pi v'^2} \right)^{\frac{1}{3}} |\Delta\mu_0|. \quad (5)$$

The main advantage of the seeding technique is that it allows for a direct ‘microscopic’ estimate of the interfacial free energy for a wide range of metastable conditions. In fact, the assumption that the nucleus is spherical can be relaxed by calculating both the nucleus shape factor and the critical nucleus size as free fitting parameters [96, 97]. In another variant of the standard approach to seeding, the committor probability,  $P_B(N_0)$ , can be fitted to obtain  $N_0^*$  at  $P_B = 0.5$  [98].

Although the seeding method improves the basic premise of CNT, it still incorporates many of the characteristic weaknesses and assumptions of CNT. Nevertheless, the seeding method has provided surprisingly accurate results for a variety of diverse systems.

Figure 3 depicts the performance of the standard seeding approach, as implemented by Espinosa et al. [78, 79], for the atomistic models TIP4P/2005, TIP4P/Ice and the coarse-grained monatomic (mW) water model. The percent supercooling for every model is defined as  $\Delta T\% = \frac{T_m - T}{T_m} \times 100$  where  $T_m$  is the melting point [36]. Evidently, seeding method calculations using the atomistic water models have yielded remarkably good agreement with experimental data for water. Theoretical results from FFS, and brute-force simulations agree with seeding calculations within error bars, with one notable exception. The nucleation rate of the TIP4P/Ice model, at a temperature of 230 K obtained from rigorous FFS calculations (filled turquoise diamond symbol in Figure 3) deviates significantly, by about 11 orders of magnitude, from both experimental results and those from seeding.

## 2 Computational Strategies for Sheared Nucleation

### 2.1 Brute-Force Approaches

Brute-force approaches constitute what is perhaps the most conceptually straightforward way of obtaining critical nucleus information, and steady-state nucleation rates. In essence, brute-force approaches involve cooling down the system below the freezing point, and performing isothermal constant-temperature simulations until a nucleation event is observed. Some manipulation is required to extract information from an ensemble of nucleation events—homogeneous nucleation is a stochastic rare event by the standards of simulations—but it should be emphasized that the dynamics of the system are not changed at all by the application of brute-force techniques.

A common strategy for generating the requisite ensemble of nucleation events is to perform several MD simulations from configurations at the same initial conditions, monitoring the time evolution of these systems until multiple nucleation events have been observed. Techniques differ in how this collection of nucleation events is processed. It should be noted that, from the methodological point of view, imposing shear on the system does not affect the general procedure adopted in brute-force approaches, although an ensemble of trajectories is required for each shear rate (and the prevailing thermodynamic conditions). The only concession required for the incorporation of shear is that sheared MD simulations must now be performed in the  $NVT$  ensemble, using the SLLOD algorithm [99] and Lees-Edwards boundary conditions [100, 101], instead of in the  $NPT$  ensemble, as is typical for MD simulations of quiescent nucleating systems.

#### 2.1.1 Rates from the Survival Probability

In an approach that closely mirrors how rates are estimated from quiescent nucleation experiments [102], induction times are calculated from an ensemble of nucleating trajectories. Induction times can be deduced from the drop in the potential energy of the system associated with the formation of the critical nucleus [103]. The induction times are then used to calculate the survival probability,  $P_{sur}(t)$ , which is the probability of finding the system in the metastable state, such that it is completely devoid of the solid phase [104]. If nucleation can be interpreted as a Poisson process [104], then the surviving probability,  $P_{sur}(t)$  can be modelled by a stretched exponential function in time,  $t$  [103]:

$$P_{sur}(t) = \exp[-(t\bar{t}_0)^{\beta'}], \quad (6)$$

where  $\bar{t}_0$  is the average induction time, and  $\beta'$  is a corrective parameter accounting for non-exponential kinetics. Both  $\bar{t}_0$  and  $\beta'$  can be gleaned from fits of the values of  $P_{sur}(t)$  to Eq. (6). The nucleation rate,  $J$ , can subsequently be calculated from the relation [104]:

$$J = \frac{1}{\bar{t}_0 V}, \quad (7)$$

where  $V$  is the volume of the liquid.

### 2.1.2 Mean First-Passage Time Method

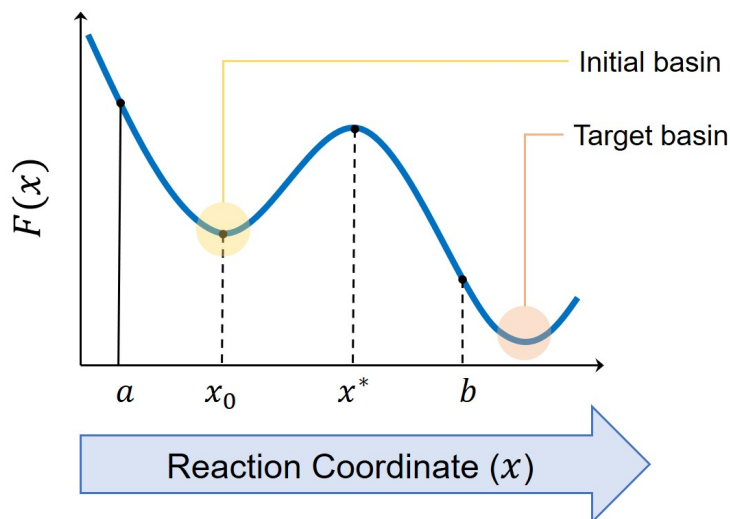


Figure 4: Schematic representation of an activated process. The reflecting boundary is at  $x = a$ , and the absorbing boundary is at  $x = b$ . The transition state,  $x^*$ , is situated at the peak of the free energy barrier which separates the initial and target basins.

The crux of this method is the assumption that the nucleation kinetics is solely controlled by the height and curvature of a sufficiently large free energy barrier. Under these conditions, growth is much faster than nucleation, and the MFPT can be directly related to the steady-state rate of barrier crossing [105]. In most treatments, the MFPT is denoted by  $\tau$ , which we abstain from in this review to avoid confusion with characteristic times associated with sheared nucleation (Section 2.3). Here, we use the notation  $T$  for the MFPT. We represent the reaction coordinate, which maps the progress of the system, by  $x$ . In the jargon of Kramer's reaction rate theory [106], the transition state,  $x^*$ , is at the top of the free energy barrier. The free energy barrier separates the initial basin, the edge of which is a reflecting boundary at  $x = a$ , and the final target basin, which yields the absorbing boundary at  $x = b$ . The system is initially "trapped" in the initial basin, at a starting point  $x_0$ . This scenario is visually depicted by Figure 4. The MFPT,  $T(x_0; a, b)$  is formally defined as the average time taken by the system, initially starting from  $x_0$ , to leave a particular domain  $[a, b]$  for the first time.

The premise of the MFPT formalism rests on certain preconditions. The activation rates, or escape rates, from  $a$  are only properly defined when the free energy barrier is sufficiently high ( $F(x^*) \gg k_B T$ , where  $k_B T$  is the thermal energy). The direct consequence of this condition is that there is a large degree of separation between the time scale of the barrier-crossing event and that of thermal diffusion; in other words, barrier-crossing is a stochastic thermally activated process. This generally holds true for homogeneous nucleation. Within this context, the MFPT,  $T(x)$ , exhibits a distinctive sigmoidal shape. The rate,  $J$ , is very simply obtained from the inverse of  $T(x^*)$ , and is agnostic to both the initial condition  $x_0$  and  $b$ .

For both sheared and quiescent homogeneous nucleation, the reaction coordinate usually chosen is the size of the largest solid cluster,  $N$ . Therefore, the analytical expression for the MFPT,  $T(N)$ , according to the MFPT formalism is given by [105]:

$$T(N) = \frac{1}{2JV} 1 + \text{erf}[c(N - N^*)], \quad (8)$$

where  $J$  is the nucleation rate,  $V$  is the total volume of the system,  $N^*$  is the critical nucleus size for a particular condition of metastability, and  $c = Z\sqrt{\pi}$ .

A description of a general implementation of the MFPT method is enumerated below:

1. The first-passage time is determined for every nucleating run. The first-passage time is defined as the time  $t$  taken for a nucleus of a particular size to first appear in a trajectory. The largest solid cluster  $N$  is determined for every saved configuration in the nucleating run under consideration. The stochastic nature of embryo size evolution implies that the time series  $N(t)$  need not be monotonic, and tends to change by increments or

decrements that are greater than unity. Skipped embryo sizes can be “filled-in” [107], so that if an embryo of a given size is observed at a certain time (say,  $t'$ ), the same time  $t'$  is assigned to smaller sizes which have not yet manifested in the trajectory. This “filling-in” procedure ensures that every nucleating run generates a first-passage time such that  $N$  changes by increments of 1 and no embryo sizes are skipped. Averaging over the first-passage times for the entire ensemble of nucleating runs yields the mean first-passage time,  $T(n)$ .

2.  $T(n)$ , is subsequently fitted to the expression given by Eq. (8).  $J$ ,  $N^*$  and  $Z$  are obtained as fitting parameters.

Luo et al. [34] calculated the sheared homogeneous nucleation rates of mW water, at a supercooling of 67.6  $K$ , using both the survival probability technique (Section 2.1.1) and MFPT (described above). Disadvantages of the brute-force approaches are immediately obvious: owing to the hefty computational cost of generating an ensemble of nucleation events using unbiased MD simulations, either the computational model or the condition of metastability must be compromised. For instance, a coarse-grained model could be chosen over more realistic models out of such practical considerations.

## 2.2 Forward-Flux Sampling

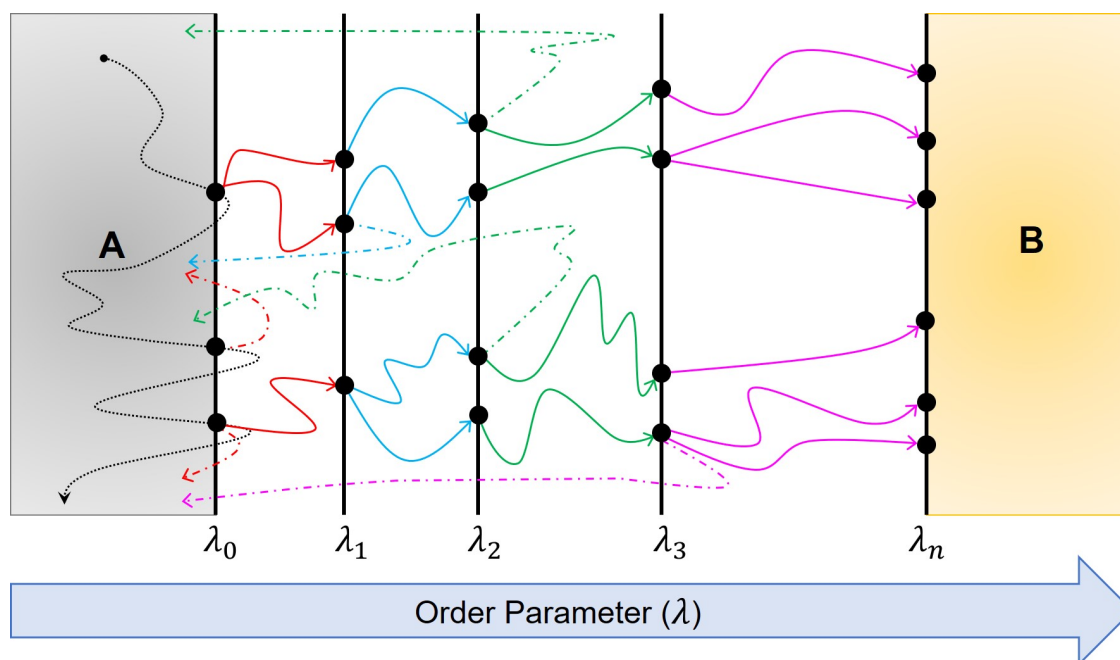


Figure 5: Schematic illustration of the DFFS algorithm [108]. The phase space between the initial state  $A$  and the final state  $B$  is partitioned by a series of  $n$  non-overlapping interfaces ( $\lambda_0, \lambda_1, \lambda_2 \dots \lambda_n$ ), defined by an order parameter  $\lambda$ . The black dotted line corresponds to the initial MD trajectory, using which the escape flux,  $\Phi$ , is calculated. Solid and dashed lines denote the successful and unsuccessful runs, respectively. Each filled black circle represents a saved configuration on a particular interface. The different colours denote the order of trial runs, coloured according to the interface from which they are launched (in successive order red, blue, green, and magenta).

Forward-flux sampling (FFS) [108, 109] is a robust path-sampling approach which is capable of simulating rare events in nonequilibrium systems with stochastic dynamics. Nonequilibrium systems are characterized by the absence of detailed balance, which means that they cannot be described by a Boltzmann-like stationary distribution and do not satisfy the condition of time reversal symmetry. These features render several rare event simulation techniques—for example, Transition Path Sampling (TPS) [110–112], Transition Interface Sampling (TIS) [113, 114], Milestoning [115, 116]—unsuitable for nonequilibrium systems. On the other hand, FFS can be used for both equilibrium and nonequilibrium systems, provided that the underlying process is Markovian. Naturally, this suggests that FFS could be an attractive option for studying sheared homogeneous nucleation. FFS and its many offshoots and flavours are covered in detail by extensive reviews [117, 118]. Here, we briefly cover the salient points of the original FFS formulation or DFFS (Direct Forward Flux Sampling) algorithm [108], pictorially depicted in Figure 5.

FFS provides a recipe for calculating the transition rate,  $k_{AB}$ , and for generating an ensemble of trajectories from an initial state  $A$  to a final state  $B$ . The transition rate, or "rate constant",  $k_{AB}$ , can be written in terms of two contributions: [113]

$$k_{AB} = \Phi P_B, \quad (9)$$

where  $\Phi$  is the escape flux, defined as the flux of trajectories which leave the initial state  $A$ , and  $P_B$  is the 'transition probability' or the probability that a trajectory departing from the initial state  $A$  reaches the final state  $B$  without returning to  $A$ .

The initial and target basins  $A$  and  $B$  are defined with respect to an appropriate order parameter,  $\lambda$ , such that if  $\lambda \leq \lambda_A$  the system is in the initial state  $A$ , and if  $\lambda \geq \lambda_B$  the system lies in the final state  $B$ . The configuration space sandwiched by the initial and final states  $A$  and  $B$  is defined by  $\lambda_A < \lambda < \lambda_B$ .

In FFS, the configuration space between an initial state ( $A$ ) and a final state ( $B$ ) is split by a sequence of non-intersecting interfaces, defined by an order parameter,  $\lambda$ . The initial state,  $A$ , is defined by  $\lambda < \lambda_A$ , and the final state,  $B$ , by  $\lambda > \lambda_B$ . However, the bottom line is that the transition probability,  $P_B$ , tends to be so small that sampling it directly using conventional brute-force simulations is prohibitive [119]. Therefore, the phase space between the basins  $A$  and  $B$  is split into a sequence of  $n$  non-intersecting interfaces,  $\lambda_i$ , such that successive interfaces lie in the direction of increasing  $\lambda$  (that is,  $\lambda_i < \lambda_{i+1}$ ), and  $\lambda_0 \equiv \lambda_A$  and  $\lambda_n \equiv \lambda_B$  (shown in Figure 5). Then  $P_B$  can be obtained from the following relation:

$$P_B = \prod_{i=0}^{n-1} p_i, \quad (10)$$

where  $p_i$  is the conditional probability that a trajectory launched from interface  $i$  reaches the next interface  $i + 1$  without returning to the initial state  $A$ . Clearly, it is much easier to sample  $p_i$  compared to the much smaller  $P_B$ . Thus, a branching ensemble of transition paths is generated via DFFS. A crucial fundamental difference between FFS and other similar path-sampling techniques is that in FFS system dynamics are integrated forward in time only, dispensing with the need for detailed balance. This in turn enables FFS to be used for nonequilibrium systems.

The DFFS algorithm was employed to analyse the sheared nucleation of a simple test case: the two-dimensional Ising model [26, 27]. Clearly, FFS is especially promising as a technique for studying sheared homogeneous nucleation because it was expressly formulated for nonequilibrium systems (while also applicable to equilibrium systems), and exploits the fluctuations of the system dynamics in the direction of the order parameter. However, a significant drawback of FFS is its prohibitive cost [118], which may make it an impractical choice for more complex systems under shear.

## 2.3 Classical Nucleation Theory Approaches

Physical intuition suggests that a linear flow field enhances the diffusion of molecules, while also injecting an additional elastic energy into the system. This class of techniques adheres to the core tenets of CNT, while incorporating modifications or extensions to account for these effects of shear. In this section, we will primarily expound recently proposed methods which quantify the elastic energy, pinpointing the free energy cost of the applied shear as a reversible elastic work term,  $W_S$ . Differences between techniques arise from how this elastic work  $W_S$ , is calculated. In the interest of clarity, we will employ a consistent system of notations for each formalism discussed below.

### 2.3.1 Rates as Functions of the Shear Rate in the Cluster Radius Space

In the framework of Mura et al. [30], the free energy cost arising from the application of a volume-preserving shear rate,  $\dot{\gamma}$ , on a solid nucleus is equated to the reversible elastic work experienced by the liquid,  $W_L$ . The applied shear rate tends to deform the solid nucleus into an ellipsoid without changing the volume contained by the nucleus. The free energy of a solid nucleus in a bulk homogeneous system, subjected to a simple shear rate,  $\dot{\gamma}$  is then given by [30]:

$$F(R) = -\frac{4}{3}\pi R^3 \frac{|\Delta\mu_0|}{v'} + 4\pi R^2 \beta\sigma_0 + \underbrace{\frac{1}{2}G(\tau\dot{\gamma})^2 \frac{4}{3}\pi R^3}_{\text{elastic work}}, \quad (11)$$

where  $F(R)$  is the free energy of formation of a cluster of radius  $R$ , and the reversible elastic work is given by  $W_L = \frac{1}{2}G(\tau\dot{\gamma})^2 \frac{4}{3}\pi R^3$ .  $\Delta\mu_0$  is the chemical potential difference between the thermodynamically stable crystal phase

and the metastable liquid phase when no shear is applied,  $\sigma_0$  is the surface tension or the interfacial free energy of the nucleus at zero shear,  $v'$  is the volume of one molecule in the crystal phase,  $G$  is the shear modulus of the nucleus. We define a characteristic time  $\tau$  [36] as  $\tau = \frac{\eta}{G}$ , such that  $\eta$  is the fluid viscosity.  $\beta = 1 + \frac{7}{24}(\tau\dot{\gamma})^2$  is a corrective "shape factor" accounting for the shear-induced change in shape of the nucleus from a sphere to an ellipsoid. For perfectly spherical nuclei,  $\beta$  is unity [30].

The radius of the critical nucleus,  $R^*$ , corresponding to the top of the nucleation barrier, obtained from Eq. (11) is:

$$R^* = \frac{2\beta\sigma_0}{\left[\frac{|\Delta\mu_0|}{v'} - \frac{1}{2}G(\tau\dot{\gamma})^2\right]}. \quad (12)$$

The corresponding free energy barrier at the critical nucleus radius,  $R^*$ , is given by:

$$F(R^*) = \frac{16\pi\sigma_0^3}{3} \frac{\beta^3}{\left[\frac{|\Delta\mu_0|}{v'} - \frac{1}{2}G(\tau\dot{\gamma})^2\right]^2}. \quad (13)$$

The steady-state nucleation rate, or current,  $J$ , across the nucleation barrier, can be determined using Kramer's escape rate theory [120, 121]. The nucleation rate is found to be:

$$J = N_{tot} \frac{\sigma_0}{k_B T} \left[8 + \frac{7}{3}(\tau\dot{\gamma})^2\right] D(R^*) e^{-\frac{F(R^*)}{k_B T}}, \quad (14)$$

where  $N_{tot}$  is the total number of particles in the metastable state, and  $D(R^*)$  is the diffusion coefficient for a critical cluster of radius  $R^*$ .

The kinetic prefactor is the quantity  $\frac{\sigma_0}{k_B T} \left[8 + \frac{7}{3}(\tau\dot{\gamma})^2\right] D(R^*)$  in Eq. (13). The kinetic prefactor can be estimated by a solution of the Smoluchowski equation in  $R$ , in the limit of small shear stresses. The calculation of the kinetic prefactor requires quantifying the effective attraction driving the attachment of particles to the crystal nucleus. Mura et al. [30] analysed a model colloidal hard sphere system using this formalism. The authors assumed that the effective attraction between a freely moving particle in the liquid phase and a particle belonging to the solid nucleus is completely described by the potential of mean force for hard spheres. The attraction was modelled as a ramp potential.

The equations explicitly incorporate shear as a dependent variable, while separating zero-shear quantities ( $\Delta\mu_0$ ,  $\sigma_0$  etc.) from flow properties and mechanical properties ( $\eta$ ,  $G$ , etc.). Consequently, it is possible to analyse the effect of shear on the nucleation rates without running simulations or performing calculations specific to any particular shear rate. Therefore, the formalism of Mura et al. [30] provides an attractive and computationally inexpensive alternative to brute-force approaches for studying the crystallization of sheared liquids. However, a mechanism was not provided within the framework for determining the interfacial energy,  $\sigma_0$ , which is generally a non-trivial calculation. In addition, the estimation of the kinetic prefactor, and specifically of  $D(R^*)$ , can become more convoluted for more sophisticated atomic potentials.

### 2.3.2 Size-Dependent Shear Moduli Calculated for Every Shear Rate

Richard et al. [122] proposed another approach, tying together seeded simulations performed at different shear rates with modified CNT equations. In the framework of Richard et al. [122], the reversible elastic work of the solid phase,  $W_S$ , is not estimated from the shear stress acting on the surrounding liquid phase,  $\nu_L = \eta\dot{\gamma}$ . Instead,  $W_S$  is calculated from simulations for every shear rate and condition of metastability. It is assumed that the nuclei or 'solid droplets' are perfectly spherical. The reversible elastic work of a nucleus of radius  $R$  and volume  $V_S = \frac{4}{3}R^3$  is given by:

$$W_S(V_S) = \frac{\nu_S^2}{2G(V_S)} V_S, \quad (15)$$

where  $G(V_S)$  is the volume-dependent shear modulus of the solid droplet, and  $\nu_S$  is the shear stress experienced by the nucleus. One of the salient features of this approach, which distinguishes it from the formalism of Mura et al. [30], is the assertion that the shear modulus of finite clusters is not equivalent to the bulk solid phase shear modulus. This is embodied by the calculation of an 'effective' shear modulus,  $G_{eff}$  for critical nuclei.

For small shear stresses, in the limit of the linear response regime, the free energy barrier height is approximated by:

$$F(\nu_S) = F_0(1 + a_W), \quad (16)$$

where  $a_W$  is a linear response coefficient, and  $F_0$  is the free energy barrier in the absence of shear.  $a_W$  is dependent on liquid and solid properties, predicted by CNT according to the expression

$$a_W = \frac{1}{G_{eff}\Delta P}, \quad (17)$$

where  $\Delta P$  is the thermodynamic driving force for nucleation, i.e., the pressure difference between the pressure inside the solid and the ambient liquid pressure.

Using the CNT prediction of  $a_W$  given by Eq. (17), the expression for the nucleation rate,  $J$ , can be obtained as:

$$\ln J \approx \ln J_0 + a_J \nu_S^2, \quad (18)$$

where  $J_0$  is the nucleation rate at vanishing stress ( $\dot{\gamma} = 0$ ), and  $a_J$  is a linear response coefficient given by  $a_J = -\Delta F_0 a_W$ .

Once  $a_W$  is known, the linear response coefficient,  $a_J$ , in Eq. (18) can be determined. Therefore, the rate calculations hinge on the estimation of the size-dependent shear modulus,  $G_{eff}$ .

For small solid droplets, the shear modulus is extracted using the following relation:

$$G_{eff} = \frac{\nu_S}{\gamma_S}, \quad (19)$$

where  $\gamma_S$  is the solid strain experienced by the solid droplets.

It is evident from Eq. (19) that the effective shear modulus can be determined once the solid density,  $\rho_S$ , shear stress,  $\nu_S$ , and solid strain,  $\gamma_S$ , have been estimated. Richard et al. [122] proposed a methodology for extracting the required statistics via seeding simulations [98], conducted at each condition of metastability, imposed  $\dot{\gamma}$ , and seed size considered.

Monodisperse hard spheres were studied using this formalism [122]. The authors validated the size-dependence of the shear modulus by showing that the shear modulus of nuclei with sizes less than 100 particles were significantly smaller than the shear modulus of the bulk crystalline phase. For such small solid droplets, the shear modulus (in reduced units) was found to be in the vicinity of  $G \approx 40$ , in comparison to the bulk shear modulus value of about 100. However, a deviation from bulk properties is not surprising, given the small size of the nuclei considered. Indeed, it is expected for small nuclei to exhibit severe finite size effects. Deformation of the solid nuclei was not considered, despite the fact that the surface area contribution to the free energy is expected to be dominant for small nuclei. Although the approach of Richard et al. [122] is conceptually rigorous, accurate, and less computationally expensive than brute-force methods, the framework may be limited in scope due to the extensive calculations required for the estimation of  $G_{eff}$  at every  $\dot{\gamma}$  considered.

### 2.3.3 Rates as Functions of the Shear Rate in the Cluster Size Space

Goswami et al. [36] proposed a formalism, similar in spirit to that of Mura et al [30]. Seeded simulations of the quiescent metastable liquid form the backbone of this formulation, wherein the shear rate appears as an explicit variable in the modified CNT expressions. The methodology involves calculating the shear-independent input quantities, along with transport properties piece-by-piece to obtain the nucleation rates as functions of the shear rate,  $\dot{\gamma}$ .

This approach builds on the expression for the free energy cost,  $F(R)$ , described by Eq. (11). The height of the free energy barrier for sheared nucleation, corresponding to a critical nucleus size  $N^*$  is given by [35]:

$$F(N^*) = \frac{N_0^* |\Delta\mu_0|}{2} \frac{\beta^3}{\left[1 - \frac{v'G}{|\Delta\mu_0|} (\tau\dot{\gamma})^2\right]}, \quad (20)$$

where  $N_0^* = \frac{32\pi\sigma_0^3 v'^2}{3|\Delta\mu_0|^3}$  is the critical nucleus size at zero shear, and  $\beta = 1 + \frac{7}{24}(\tau\dot{\gamma})^2$  is the shape factor correcting for ellipsoidal deformation.

The steady-state nucleation rate,  $J$ , can be derived from Zeldovich-Frenkel equation [38, 46], yielding the following familiar CNT-based expression [35]:

$$J = \rho_l Z f^+ e^{-\frac{F(N^*)}{k_B T}}, \quad (21)$$

where the nucleation rate  $J$  is the current or flux across the free energy barrier, in the cluster-size space and is in units of the number of nucleation events per unit volume per unit time,  $f^+$  is the rate of attachment of particles to the critical cluster,  $\rho_l$  is the number density of the supercooled liquid,  $Z$  is the Zeldovich factor, and  $(\rho_l Z f^+)$  is the kinetic prefactor. This rate equation is an analogue of Eq. (3). However, here,  $Z$ ,  $f^+$ ,  $N^*$  are functions of the shear rate,  $\dot{\gamma}$ .

The attachment rate depends on the two-dimensional diffusion coefficient,  $D_l$ , which in turn depends on the magnitude of  $\dot{\gamma}$  at a particular temperature  $T$ . It has been shown that atomic systems and suspensions [123, 124] follow a linear relationship with  $\dot{\gamma}$ , given by:

$$D_l = D_0 + c\dot{\gamma}, \quad (22)$$

where  $D_0$  is the diffusion coefficient at zero shear rate for the quiescent liquid at a particular  $T$ , and  $c$  is a fitting parameter with units of squared length.

Using scaling arguments, the transcendental expression for  $J$  can be approximated by a polynomial function in  $\dot{\gamma}$ , valid for shear rates for which Eq. holds true,  $\dot{\gamma} < \frac{1}{\eta} \left( \frac{2G|\Delta\mu_0|}{v'} \right)^{\frac{1}{2}}$ , and  $\beta \approx 1$  [36].

$$J = J_0 \left( 1 + \frac{c}{D_0} \dot{\gamma} \right) \left[ 1 - \frac{N_0^* v' G}{2k_B T} (\tau \dot{\gamma})^2 \right], \quad (23)$$

where  $J_0$  is the nucleation rate when the shear rate is zero.

The form of Eq. (21), and more transparently, that of Eq. (23) suggest that, at a particular temperature, there exists a maximum in the nucleation rate at a specific shear rate,  $\dot{\gamma}_{opt}$ . An estimate of the dimensionless optimal shear rate,  $\tau \dot{\gamma}_{opt}$  can be derived analytically, for  $\frac{6c^2 G k_B T}{N_0^* v' (D_0 \eta)^2} \ll 1$  [36]:

$$\tau \dot{\gamma}_{opt} = \left( \frac{k_B T}{D_0 \eta} \frac{c}{v'} \right) \times \frac{1}{N_0^*}, \quad (24)$$

where the dimensionless group defined as  $B = \left( \frac{k_B T}{D_0 \eta} \frac{c}{v'} \right)$  is related to the transport properties ( $\eta$  and  $D_0$ ).  $N_0^*$  is dependent on the thermodynamic properties ( $\Delta\mu_0$ ,  $\sigma_0$  etc.). The dimensionless product,  $\tau \dot{\gamma}_{opt}$ , is an intrinsic measure of how the temperature affects the variation of the nucleation rates with  $\dot{\gamma}$ .

A crucial difference between the approach of Goswami et al. [35, 36] and that of Richard et al. [122] is that seeded simulations must be performed for every shear rate in the case of the latter, while for the former only seeded simulations at zero shear are required. In addition, the crux of the methodology of Richard et al. [122] is that the size dependent shear modulus,  $G_{eff}$ , is appreciably divergent from the bulk crystal shear modulus.

Interestingly, Goswami et al. [36] found that predictions from their formalism agreed very well, within error bars, with brute-force MFPT calculations for the mW water model at 207 K [34] (corresponding to a supercooling of 67.6 K).

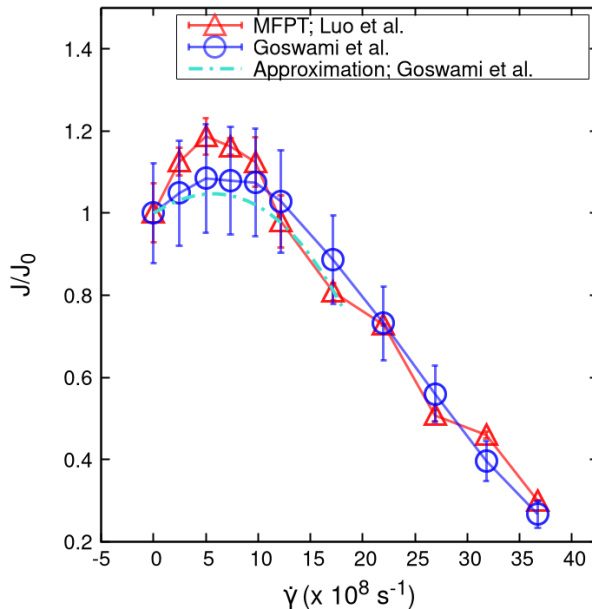


Figure 6: Comparison of  $J/J_0$  for the mW model at a supercooling of  $67.6 K$ , estimated using the formalism of Goswami et al. [35, 36] (open blue circles) with the MFPT results (open red triangles) of Luo et al [34]. The polynomial approximation (Eq. (23)), depicted as a turquoise dashed line, agrees well with both sets of results.

Figure 6 shows a comparison of the scaled nucleation rates,  $J/J_0$ , obtained using MFPT by Luo et al. and those calculated using Eq. (21) and Eq. (23). Even the simple approximation described by Eq. (23) shows high fidelity with calculations performed using Eq. (21), within the range of applicability.

While the magnitude of  $J_0$  depends solely on thermodynamic quantities, including  $\Delta\mu_0$  and  $\sigma_0$ , the shear dependent  $J$  is influenced by shear-dependent quantities, and the ratio  $J/J_0$  reveals the effects of shear on the nucleation rates. Finite size effects, due to the size-dependent shear modulus and density within the nuclei would presumably affect the variation of  $J/J_0$ . However, the good agreement with MFPT calculations shown in Figure 6 suggests that the disparity in the bulk modulus of finite clusters, reported by Richard et al. [122] for hard spheres, does not significantly detract from the predictive power of the formalism of Goswami et al. [36], at least for mW water, considering  $N_0^*$  values of about 70. Finite-size effects are expected to be even less significant for larger  $N_0^*$ , corresponding to more realistic supercoolings.

In an earlier work on colloidal suspensions [15, 16], results from equilibrium umbrella sampling calculations and non-equilibrium Brownian simulations were fitted empirically to functions of  $\dot{\gamma}$ . Shear-dependent  $\Delta\mu$  and  $\sigma$  were obtained, which were subsequently substituted in the original CNT equations (Section 1.1). The expressions for the ‘effective’ chemical potential and interfacial energy are given by:

$$|\Delta\mu| = |\Delta\mu_0|(1 - c_0\dot{\gamma}^2), \tag{25}$$

$$\sigma = \sigma_0(1 + \kappa_0\dot{\gamma}^2), \tag{26}$$

where  $c_0$  and  $\kappa_0$  are positive coefficients.

The governing equations of both Mura et al.[30] and Goswami et al.[35] are consistent with this description: quadratic functions of  $\dot{\gamma}$  can be defined for the effective  $\Delta\mu$  and  $\sigma$ , in terms of  $\Delta\mu_0$  and  $\sigma_0$ , respectively. Accordingly, the values of the coefficients from both these approaches are  $c_0 = \frac{1}{2}Gv'\tau^2$  and  $\kappa_0 = \frac{7}{24}\tau^2$ .

### 3 Results from Simulations and Theory

#### 3.1 Effects of Shear on Energetics, Kinetics and Nucleation Rates

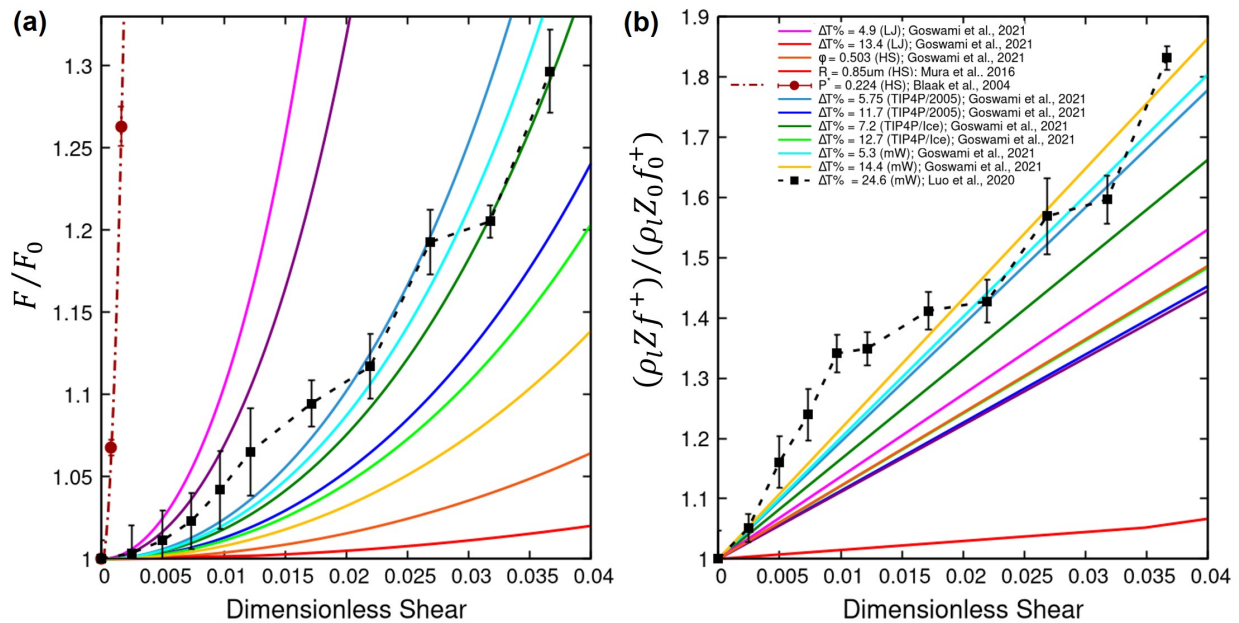


Figure 7: (a) Increase of the normalized free energy barrier height,  $F/F_0$ , with shear. (b) Variation of the normalized kinetic prefactor,  $(\rho_l Z f^+)/(\rho_l Z_0 f_0^+)$ , with respect to the dimensionless shear rate. Trends for LJ, HS, colloids, atomistic water models (TIP4P/2005 and TIP4P/Ice), and the coarse-grained mW water model have been shown at several metastable conditions, using the results of Blaak et al. [15, 16], Mura et al. [34], Luo et al [34], and Goswami et al [36]. Here,  $\Delta T\%$ ,  $P^*$ ,  $R$  denote the percent supercooling [36], the pressure in reduced units for colloids [15, 16], and the radius of the hard spheres considered [30], respectively. The shear rates are multiplied by  $\tau = \eta/G$  to obtain the dimensionless shear unless nondimensionalized shear rates are reported [30, 34, 36]. For the mW model, at a percent supercooling of 24.6% (filled black squares),  $\eta = 30.94 \text{ mPas}$  [36] and  $G = 3.1 \text{ GPa}$  [125] have been used.

From a molecular standpoint, a steady flow has complex energetic and kinetic effects on the process of sheared homogeneous nucleation. CNT-based approaches and MFPT conveniently split these shear contributions into distinct trends affecting two separate quantities, which can be analyzed independently: the free energy barrier and the kinetic prefactor.

Figure 7(a) depicts the variation of the free energy barrier with shear, drawing from various results on Lennard-Jones (LJ), hard spheres (HS), colloids, and water models [15, 30, 34, 36]. Clearly, the free energy barrier height increases with increasing shear for every system considered, irrespective of the specific methodology employed. Blaak et al [15, 16]. showed that the free energy barrier is a quadratically increasing function of shear for colloids modelled with Yukawa repulsion, which is a trend that is qualitatively supported by subsequent studies on several other systems (Figure 7(a)). Further, we note that the increase in the free energy is also heralded by the dependence on  $\dot{\gamma}$  in Eq. (13) and Eq. (20). A physical interpretation of this scenario is that the imposed shear induces a small elastic deformation in the solid nucleus, which incurs an additional free energy cost, thereby enlarging the free energy barrier height (compared to the quiescent nucleation free energy). The concomitant increase in the critical nucleus with shear can also be rationalized by the shear deformation of the nucleus [15, 30, 34–36, 126].

On the other hand, the kinetic prefactor is the embodiment of the kinetics of the sheared nucleation process. Figure 7(b) shows the increase of the kinetic prefactor with increasing shear, which is a natural consequence of the shear-enhanced motions of particles.

We surmise that the height of the free energy barrier and the kinetic prefactor both tend to increase continuously with increasing  $\dot{\gamma}$ , at a specific condition of metastability (for example, the prevailing  $T$ ,  $P$  or  $\phi$ ). These trends indicate the existence of a maximum in the nucleation rate,  $J$ , at a particular value of  $\dot{\gamma}_{opt}$ . For shear rates such that  $\dot{\gamma} < \dot{\gamma}_{opt}$ , the

kinetic enhancement dominates the extra energetic cost arising from elastic deformation of the solid nucleus, and  $J$  increases.  $J$  reaches its peak value at the optimal shear rate,  $\dot{\gamma}_{opt}$  (at the thermodynamic metastability condition  $T, P$  or  $\phi$ ). However, when the applied  $\dot{\gamma} > \dot{\gamma}_{opt}$ , the energetic effects of shear overpower the kinetic increase, and  $J$  decreases. This mechanism is corroborated by the non-monotonic behaviour of  $J$  with  $\dot{\gamma}$ , independent of the calculation method employed, reported for the sheared two-dimensional Ising model [26], colloidal models [28, 29], hard spheres [30, 36, 127], glassy systems [31, 32], a binary-alloy [33], more recently mW water under shear [34–36], and LJ and atomistic water models [36].

### 3.2 Temperature Dependence

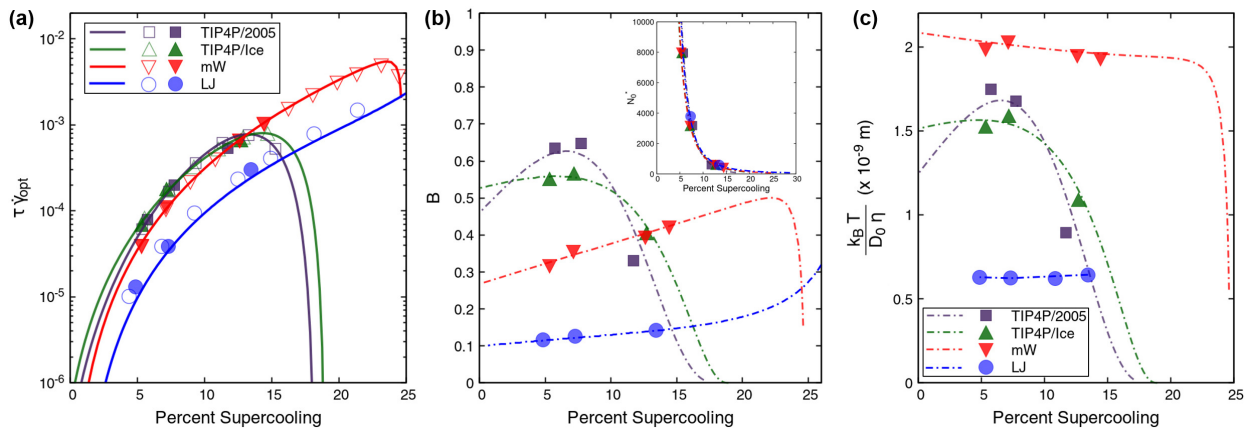


Figure 8: (a) Variation of the dimensionless  $\tau\dot{\gamma}_{opt}$  with the percent supercooling,  $\Delta T\%$ , for atomistic water models, the mW water model and LJ. (b) Change in the dimensionless quantity,  $B = \left(\frac{k_B T}{D_0 \eta} \frac{c}{v'}\right)$ , with  $\Delta T\%$ . The inset depicts the more-or-less 'universal' trend of  $N_0^*$  with  $\Delta T\%$ . (c) Evaluation of the validity of the Stokes-Einstein (SE) relation, which states that  $\frac{k_B T}{D_0 \eta}$  is constant with respect to temperature. The SE relation is violated for the water models, at deep supercoolings. Filled markers, open symbols and dashed lines denote results from simulation data, calculations using fitted equations to simulation data, and estimations from the approximate expression of Eq. (24), respectively. Reproduced with permission from Goswami et al [36]. Copyright 2021 American Physical Society.

The dependence of the nucleation rate for quiescent systems,  $J_0$ , on  $T$  can be ascertained by using fits to the CNT expression (Eq. (3)) [78, 79]. The trend of  $J_0$  with  $T$  for various water models is shown in Figure 3.

However, the homogeneous sheared nucleation rate,  $J$ , is controlled by several shear and temperature dependent parameters. To examine the dual influences of temperature and shear, the dimensionless product,  $\tau\dot{\gamma}_{opt}$  (given by Eq. (24)) was analyzed for water and LJ, using a CNT-based approach (described in Section 2.3.3) [36]. The dimensionless optimal shear,  $\tau\dot{\gamma}_{opt}$ , can be considered to be a measure of the relative 'shift' of scaled nucleation rate curves (each at a particular temperature), with shear. The percent supercooling,  $\Delta T\%$ , provides a convenient system-agnostic measure of the supercooling [36].

Figure 8(a) shows the variation of  $\tau\dot{\gamma}_{opt}$  with  $\Delta T\%$  for the TIP4P/2005, TIP4P/Ice, mW and LJ models. It is strikingly apparent that the water models exhibit different behaviour from that of LJ:  $\tau\dot{\gamma}_{opt}$  is non-monotonic with  $\Delta T\%$  for water. This translates to the non-monotonic behaviour in the optimal shear rate,  $\dot{\gamma}_{opt}$ , with temperature, for each water model. This non-monotonicity was purported to be a new anomaly of water [36]. To investigate the cause of this anomalous trend, the two constituent groups,  $B$  and  $N_0^*$ , in Eq. (24) were analyzed. It was found that  $B$  reflected the observed trends of  $\tau\dot{\gamma}_{opt}$ , while the variation of  $N_0^*$  with  $\Delta T\%$  was almost identical for both water and LJ, as depicted in Figure 8(b).

Water is notoriously peculiar compared to most simple liquids, exhibiting several anomalies in the supercooled regime [128]. One of the most well-known anomalies in the dynamics of supercooled water is the breakdown of the Stokes-Einstein (SE) relation. The SE relation asserts that  $\eta$  and  $D_0$  are coupled such that  $\frac{k_B T}{D_0 \eta}$  is constant with temperature [129, 130]. Interestingly, the origin of the non-monotonicity in  $\tau\dot{\gamma}_{opt}$  was directly traced to the violation of the SE relation [36], shown in Figure 8(c). The results suggest that, in general, any system violating the SE relation

(including glass-forming liquids, and simple liquids near the glass transition) will exhibit the same anomaly, that is, non-monotonicity of  $\tau\dot{\gamma}_{opt}$  with temperature.

### 3.3 Dependence of Supersaturation

Colloidal suspensions are often modelled by hard sphere particles. For HS, the packing fraction  $\phi$ , indicating the degree of supersaturation, is the condition of metastability dictating quiescent nucleation. Therefore,  $\phi$  is analogous to the conditions of metastability— $T$  or  $P$ —for atomic systems [30]. The dependence of the rich quiescent nucleation behaviour of HS on  $\phi$  has been well-documented in the literature. Phase transitions from the disordered fluid state to crystal state take place in the packing fraction range  $0.492 < \phi \leq 0.545$  [131–135]. Two regimes for quiescent nucleation were discovered, for low and high supersaturations [136–139]. At lower concentrations ( $\phi < 0.56$ ), standard nucleation and growth were observed. At higher concentrations ( $\phi > 0.56$ ) a spinodal-like nucleation regime was determined, wherein the free energy barrier is virtually negligible.

Interestingly, the same crossover packing fraction,  $\phi = 0.56$ , resolves the sheared homogeneous nucleation behaviour of HS into two separate regimes. Richard et al [127] examined the sheared homogeneous nucleation of monodisperse HS, for various  $\phi$ . The chosen shear rates ( $0 < \dot{\gamma} \leq 1.414$ , where  $\dot{\gamma}$  is in reduced units) were smaller than those required for shear-induced ordering [140]. Two distinct regimes were identified, corresponding to low and high supersaturation: 1) suppression of crystallization, for  $\phi \leq 0.56$ , and 2) crystallization enhancement, in the range of  $0.56 < \phi \leq 0.587$ . The results clearly indicate that the supersaturation plays a pivotal role in the sheared homogeneous nucleation of HS. It is likely that supersaturation and polydispersity are crucial factors governing the sheared nucleation of hard-sphere colloids and colloidal glasses.

### 3.4 Structural Effects of Shear

The structural consequences of shear on solid nuclei can be broadly delineated into two related effects: changes in the overall shape, and shear-induced changes in the microscopic structure of incipient nuclei.

#### 3.4.1 Shear-Induced Changes in Nucleus Shape

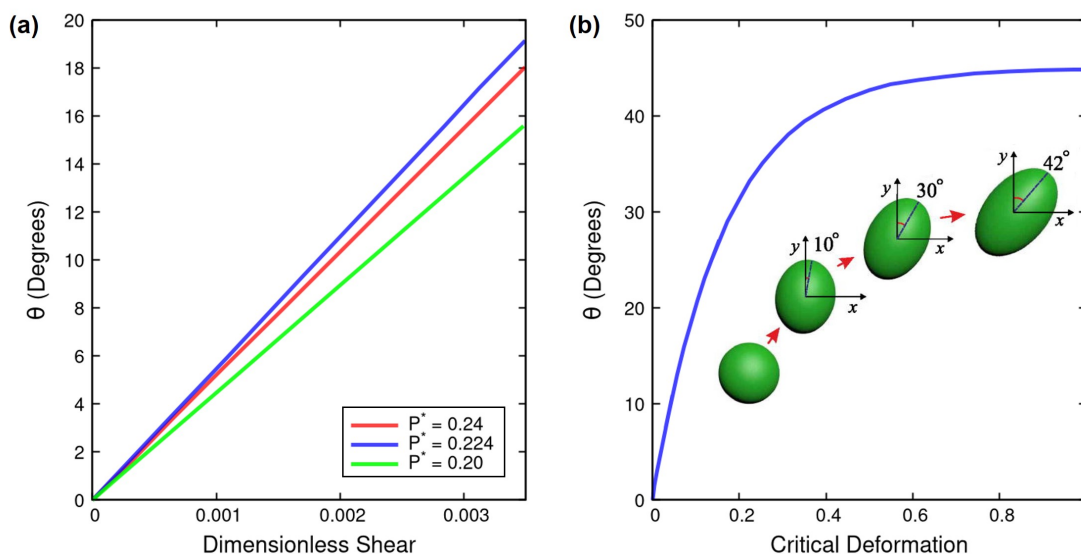


Figure 9: (a) The tilt angle,  $\theta$ , plotted against the dimensionless shear for a colloidal system at various pressures (in reduced units), taken from Blaak et al [15, 16]. The shear flow is in the  $x$ -dimension. (b) Power law fits of the tilt angle,  $\theta$ , to data for a model glassy system, at various temperatures, as a function of the critical deformation [141]. The critical deformation is defined as the deformation of a critically sized nucleus, which is a dimensionless quantity. The insets depict visualizations of the change in the orientations and shape of the critical nuclei. The direction of the applied shear, and the shear gradient are the  $x$  and  $y$  directions, respectively. Reproduced from Galimzyanov et al. [141], with the permission of AIP Publishing.

Changes in the shape of solid nuclei due to an imposed flow field have been hypothesized, modelled and reported in theory, simulations, and experiments for diverse systems, notably including polymers [142–145].

The formation of elongated nuclei was observed in Brownian dynamics simulations of colloids, which were deformed such that their largest dimension was preferentially aligned along the direction of vorticity [15, 16]. Kinetic Monte-Carlo simulations of polymer melts under shear revealed the growth of non-spherical nuclei in the so-called "shish-kebab" morphology [18, 142–144, 146, 147]. On the other hand, the shape factor,  $\beta$ , (Section 2.3.1) was designed to theoretically account for the ellipsoidal deformation of spherical nuclei in sheared simple liquids. Ellipsoidal shape deformations were also found to occur for single-component glassy systems [141].

The tilt angle,  $\theta$ , is defined as the angle between the shear-gradient direction and the longest axis of a solid ellipsoidal nucleus [15]. Figure 9(a) and Figure 9(b) represent how the shapes of nuclei are altered due to a simple linear flow applied in the  $x$  direction, for colloids [15, 16] and a glassy system [141], respectively. Unsurprisingly, the shape deformations are more pronounced for higher shear rates for both systems. We conclude that anisotropy in the shape of nuclei is expected to be more prominent at high shear rates. It stands to reason that computational approaches which assume perfectly spherical nuclei under the action of shear should be applied in the regimes of 'low' shear rates where these shape deformations are less significant.

### 3.4.2 Shear-Induced Changes in Microscopic Structure

The application of a simple shear rate,  $\dot{\gamma}$ , imparts an elastic deformation to a solid nucleus. It is not a stretch of logic to expect that a mechanical deformation would also affect the internal microscopic structure of emerging solid nuclei. The analysis of microscopic structures is impervious to CNT-based approaches which, in fact, usually neglect structural effects completely in rate calculations. However, stacking faults and fivefold defect structures [148], detected during the quiescent nucleation of supercooled water [149–151], have been found to emerge as precursors to nucleation, even before critical nuclei appear [87]. Furthermore, there is long-standing evidence that morphological and structural characteristics of emergent crystalline structures have a non-trivial impact on the sheared nucleation process [152]. Theoretical inferences notwithstanding, the possibility of shear affecting nascent crystal defect structures, thereby influencing the nucleation pathway, has not yet been explored for sheared homogeneous liquid-to-solid phase transitions of simple liquids.

In this review, we have mainly focussed on the effect of a constant simple shear rate on liquid-to-solid homogeneous phase transitions. However, amorphous or disordered solid states can also undergo solid-to-solid phase transitions. Deeply supercooled glassy systems may be heated up (vitrification) or subjected to mechanical stress or shock to aid the internal structural reshuffling required for a solid phase transformation [153]. Shear-induced amorphous crystal phase transformations have been investigated using experiments [22] and brute-force simulation approaches, for single-component LJ systems [154, 155], a model metallic glass [17], and relatively stable disordered systems like amorphous silicon ( $a - \text{Si}$ ) [156]. Such solid-to-solid phase transitions are qualitatively distinct from phase transitions from the liquid state, and exhibit intriguingly intricate phase behaviour. Employing molecular dynamics simulations on a model of  $a - \text{Si}$ , Kerrache et al [156], identified three different regimes of shear-induced structural reorganization: (i) formation of a more disordered state, rich in fivefold liquid-like atoms at low temperatures or high shear rates, (ii) the formation of an annealed state when thermal effects dominate the effects of shear deformations, and (iii) the creation of a crystalline solid phase. It is evident that subtle structural changes dictate the nature of these solid-to-solid phase transitions, although perhaps a path-sampling technique like FFS (alluded to in Section 2.2) might be capable of determining mechanisms of the proposed pathways.

### 3.5 Polymer Crystallization under Shear

This review has concentrated mostly on how shear affects the homogeneous nucleation of 'simple' metastable liquids (for example, LJ and water), HS colloids and glassy systems. The flow-induced crystallization (FIC) of polymers is an intriguing nonequilibrium kinetically controlled phase transition [18] that is of immense technological importance [157–160]. However, the study of the crystallization of polymers is fraught with considerably greater complexity, arising from the several levels of structural organization that can characterize such phase transitions. In Section 3.4, we alluded to how strongly aligned, elongated nuclei, called "shish-kebabs", form in sheared polymer melts, which are drastically different from the ellipsoidal nuclei formed in simple liquids and glassy systems. The difference in morphology is made explicit in Figure 10. The crystallization process of polymer melts differs fundamentally from that in simple liquids due to the interactions and associations of constituent chains. Figure 10(a) pictorially depicts the various addition mechanisms of polymer segments to the nucleus, according to the coarse-grained Graham and Olmsted (GO) [18, 161] model. Entanglement of polymer chains refers to the topological impediment of molecular motion by other chains [162, 163], which could also be relevant for nucleation. Here, we briefly outline key conclusions. FIC is discussed in more detail elsewhere [164–168].

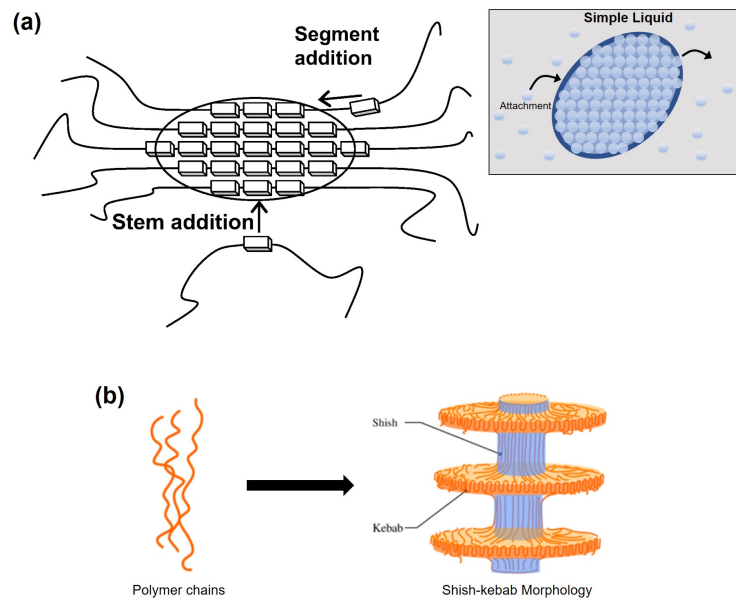


Figure 10: (a) Schematic of the mechanism of polymer nucleus growth, as modelled by the coarse-grained GO model [18, 161]. Reproduced from Ref [165] by permission of The Royal Society of Chemistry. The inset depicts the attachment (and detachment) of molecules or particles, schematically represented by circles, to a shear-deformed ellipsoidal nucleus, according to CNT-based approaches [30, 36, 122]. (b) Pictorial representation of the non-spherical "shish-kebab" morphology characteristic of sheared nucleation in polymers. Adapted with permission from Ref [147]. Copyrighted by the American Physical Society.

Model alkane systems are an illustrative example of the intricacies involved in polymer crystallization. In a study of the sheared nucleation of short chain alkanes,  $n$  – eicosane (henceforth referred to as C20) and  $n$  – hexacontane (C60), the application of a planar shear flow was found to speed up crystallization and enhance the crystal growth rate [169]. It was also concluded that the chain length is directly linked with the magnitude of the ‘critical shear rate,’ defined as the shear rate above which crystallization is enhanced by shear. An inference that can be drawn is that the relaxation time of the molecules is related to the susceptibility to shear-induced crystallization [169, 170].

Using NEMD simulations, Anwar et al [171]. studied the quiescent and sheared nucleation of the short chain alkane,  $n$  – eicosane (C20) and a long chain alkane,  $n$  – pentacontahexane (C150), at 20 – 30% undercooling. Under quiescent conditions, it was found that nucleation proceeds according to the same mechanism for both the long and short chains: the chain segments sequentially first align, straighten, and then coagulate into clusters. For low shear rates, the authors discovered that both the long and short chains obey the same nucleation mechanism as that of quiescent nucleation. Conversely, at high shear rates, a difference in behaviour was observed for C20 and C150. Chains of C20 simultaneously align and straighten, which is followed by a local increase in density. In contrast, C150 chains follow the same sequence of events as those in quiescent nucleation. These observations are consistent with both experiments and theory [172].

A recent NEMD study on the crystallization of entangled linear polymer chains (C1000), consisting of 1000 monomers, investigated the interplay of entanglement, shear and temperature [173]. A more pronounced effect of the imposed shear rates was found on the C1000 chains at higher temperatures. A weak dependence of the induction strain (defined as the product of the nucleation induction time and shear rate) on the shear rate was also determined.

Clearly, flow can play a crucial non-trivial role in polymer crystallization. The generally accepted consensus of the molecular effects of shear is that an applied flow unravels and stretches polymer chains, which are initially in a quiescent random-coil configuration, thereby inhibiting their conformational freedom. This enables the polymer chains to assemble in the elongated configurations that are precursors to crystallization. Capturing these events is the primary challenge of modelling polymer systems in simulations. Brute-force approaches and rare event biasing techniques, often paired with an appropriate computational model (for example, the GLaMM model [174], and the GO model [18, 161]), are generally the techniques of choice employed. It is not yet clear if a phenomenological theory (like the CNT-based approaches discussed for simple liquids) can be suitably modified for polymer crystallization. Although FFS has been utilized for structural relaxation and translocation of quiescent polymers [175–180], determining adequate

order parameters for describing the complex process of sheared polymer crystallization, which typically involve the registry of polymer chains and elongation of nuclei under flow, could be especially daunting.

### 3.6 Purview of Experiments

Water is ubiquitous and widely studied, which we consider first as a representative member of the class of simple liquids. The homogeneous quiescent nucleation of ice is often estimated by droplet experiments [92, 181–185], wherein the homogeneous nucleation rate is generally equated to the volume nucleation rate. Nucleation experiments of water are hampered by the notorious "no-man's land" [186], which sets a practical limit to the supercooling that can be achieved, due to rapid ice crystallization that prevents characterization of the phase transformation. The border no-man's land, situated at around 227 – 228 K, has been penetrated by subversive studies aided by advanced cutting-edge technologies [182, 185, 187–191]. However, in general, experimentally accessible supercoolings are low or moderate within the scope of simulations and theory, which perhaps contributes to the infamous divide between computational results and experiments [9, 192, 193].

In crystallization experiments, shear can be imposed via a Couette cell [194], Taylor-Couette flow system [25, 195], Capillary setup [20], viscometer [196–199], rheometer [200], short-term shearing approaches [201–204] and microfluidics [23]. In general, equipment used in sheared crystallization experiments can be classified into two categories: capillary and rotational devices [23]. In a capillary device, the pressure difference in a capillary is used to create high shear rates of up to  $3 \times 10^5 \text{ s}^{-1}$  for short millisecond length bursts of operation. Unfortunately, a range of shear rates are imposed instead of a constant shear rate due to the pressure-driven Poiseuille flow. Rotational devices attempt to generate a Couette flow but risk creating turbulent flows at higher shear rates [205] and inhomogeneous flows. On the other hand, microfluidic devices impose flows with low Reynolds numbers (and consequently impose low shear rates), eliminating the possibility of turbulent flows [23]. By contrast, Couette-Taylor devices rely on turbulent flows to enhance mixing [206].

The nature of these disparate experimental techniques naturally leads to the conundrum of how a uniform shear rate can be imposed while subjecting the system to the supercoolings required for the nucleation of water, and by extension, other simple liquids. It seems likely that temperatures within no-man's land will certainly be out of reach of conventional Couette flow type experiments.

On the other hand, analysing the sheared nucleation of dense suspensions, colloids, polymers and proteins presents less serious challenges from the point of view of experiments. Experimental aspects of FIC of polymers has been extensively reviewed in previous work [166, 167]. Recent theoretical results on a colloidal suspension of PMMA (poly(methyl methacrylate)) indicate that colloids, subjected to a constant linear flow, will exhibit non-monotonicity in the nucleation rate within shear rates of a few seconds inverse [30]. Imposing such linear flows are well-within the capabilities of the arsenal of modern experimental techniques, at ambient temperatures.

### 3.7 Future Scope and Challenges

Brute-force approaches (of which MFPT is primarily used for sheared homogeneous nucleation) are straightforward in application and can provide unbiased estimates if sufficiently good statistics are obtained. Unfortunately, the spatio-temporal resolution of unbiased MD simulations dictates that obtaining the requisite ensemble of nucleating trajectories is computationally very expensive. In fact, brute-force approaches are infeasible for systems which do not nucleate within achievable simulation times. Furthermore, every imposed shear rate necessitates generating a separate ensemble of trajectories. For example, if  $J$  values at 4 different shear rates are desired, it can be surmised that at least 4 times the computational cost of estimating  $J_0$  at the same thermodynamic conditions will be incurred. Therefore, calculations at moderate and low supercoolings, for a finite number of shear rates are not yet practically feasible, and usually only deep supercoolings can be studied using brute-force approaches.

CNT-based approaches describing sheared homogeneous nucleation are relatively less expensive, and work reasonably well for several systems over a wide range of metastabilities. The simple governing expressions facilitate general analyses and enable overarching inferences to be drawn for a variety of conditions. However, CNT involves considerable approximations, even when augmented with seeded simulations and other methodological improvements. Qualitative agreement notwithstanding, CNT-based techniques are fundamentally impaired by the very assumptions that impart this class of methods with their trademark simplicity.

FFS could be an attractive alternative, and is known to provide reliable insight into microscopic structures, preferred pathways, and molecular mechanisms. FFS is certainly a promising approach, but though FFS is 'embarrassingly parallel' it remains computationally exorbitant [118]. FFS has the same fatal flaw as brute-force approaches: a bundle of trajectories must be generated for every shear rate of possible interest. Perhaps this is why, till date, only the sheared

two-dimensional Ising model has been analysed using FFS, to the best of our knowledge [26, 27]. A viable strategy might be to pair FFS with other less costly computational approaches to identify shear regimes of interest.

Another point illuminated by recent work on water [34–36] is that the optimal shear rates, at moderate and deep supercoolings, are several orders of magnitude greater than shear rates that can be imposed by experiments. Water is an exemplary example: generating a constant linear velocity profile within no-man’s land may not be feasible in experiments. Adding to this difficulty is the increased uncertainty of simulation results for lower shear rates which are experimentally achievable [34]. This may be one of the contributing factors for why the non-monotonic behaviour of  $J$  with  $\dot{\gamma}$ , predicted by simulations and theory, has not yet been observed in experiments of simple Newtonian liquids.

Shear can cause a plethora of interesting effects in polymers melts and glasses, including jamming transitions, annealing, shear-induced ordering etc. Brute-force approaches and coarse-grained models are typically used for analysing the effects of flow on polymer phase transitions. It remains to be seen whether CNT pathways and the theoretical models developed for simple liquids can be applied to study the complex rheological behaviour of polymer melts.

Although we have not discussed sheared heterogeneous nucleation in this review, a recent study on mW water showed that the sheared heterogeneous nucleation rates are also non-monotonic with shear [207]. Unbiased MD simulations were used by the authors, but brute-force approaches are not always feasible, even for heterogeneous nucleation [9]. On the other hand, it could be possible to extend CNT-based approaches to heterogeneous nucleation, which would presumably be applicable to a wider variety of systems and surfaces. Heterogeneous CNT methods, relying on random structure searches [208] and machine learning [209], have been proposed and employed for quiescent nucleating systems. Though the prospect of a CNT-based approach for sheared heterogeneous nucleation is appealing, seemingly insurmountable challenges are also involved. A rigorous theoretical treatment of the exotic flow field around a nucleus sitting on a surface may not be tractable. In addition, while the internal structures and polymorphic diversity of nuclei are usually ignored for homogeneous nucleation, the microstructure may be significant for heterogeneous nucleation.

It is abundantly clear that the sheared homogeneous nucleation of Newtonian liquids, dense suspensions, glassy systems, and polymer melts exhibits richly diverse and complex phase behaviour. Theory and simulations can be particularly relevant for studying the elusive sheared homogeneous nucleation of simple liquids and glassy systems, especially for high shear rates which are beyond the current capabilities of Couette flow inducing experiments. We hope that computational techniques and theoretical tools will be developed further, striving towards greater fidelity with available experimental data and contributing to our understanding of the fascinating phenomenon of nucleation under flow.

## 4 Acknowledgements

This work was supported by the Science and Engineering Research Board (sanction number STR/2019/000090 and CRG/2019/001325).

## References

1. Chayen, N. E., Saridakis, E. & Sear, R. P. Experiment and theory for heterogeneous nucleation of protein crystals in a porous medium. *Proceedings of the National Academy of Sciences* **103**, 597–601 (Jan. 2006).
2. Ken Kelton, A. L. G. *Nucleation in Condensed Matter: Applications in Materials and Biology* (ed Greer, A. L.) (Elsevier, 2010).
3. Lee, A. Y., Erdemir, D. & Myerson, A. S. Crystal Polymorphism in Chemical Process Development. *Annual Review of Chemical and Biomolecular Engineering* **2**, 259–280 (July 2011).
4. Bartels-Rausch, T. Ten things we need to know about ice and snow. *Nature* **494**, 27–29 (Feb. 2013).
5. Murray, B. J. *et al.* Heterogeneous nucleation of ice particles on glassy aerosols under cirrus conditions. *Nature Geoscience* **3**, 233–237 (Mar. 2010).
6. Zhang, Z. & Liu, X.-Y. Control of ice nucleation: freezing and antifreeze strategies. *Chemical Society Reviews* **47**, 7116–7139 (2018).
7. Murray, B. J., O’Sullivan, D., Atkinson, J. D. & Webb, M. E. Ice nucleation by particles immersed in supercooled cloud droplets. *Chemical Society Reviews* **41**, 6519 (2012).
8. Tanaka, K. K. & Kimura, Y. Theoretical analysis of crystallization by homogeneous nucleation of water droplets. *Physical Chemistry Chemical Physics* **21**, 2410–2418 (2019).
9. Sosso, G. C. *et al.* Crystal Nucleation in Liquids: Open Questions and Future Challenges in Molecular Dynamics Simulations. *Chemical Reviews* **116**, 7078–7116 (May 2016).
10. Penkova, A., Pan, W., Hodjaoglu, F. & Vekilov, P. G. Nucleation of Protein Crystals under the Influence of Solution Shear Flow. *Annals of the New York Academy of Sciences* **1077**, 214–231 (Sept. 2006).

11. Woodhouse, F. G. & Goldstein, R. E. Cytoplasmic streaming in plant cells emerges naturally by microfilament self-organization. *Proceedings of the National Academy of Sciences* **110**, 14132–14137 (Aug. 2013).
12. Berland, C. R. *et al.* Solid-liquid phase boundaries of lens protein solutions. *Proceedings of the National Academy of Sciences* **89**, 1214–1218 (Feb. 1992).
13. Baird, J. A., Santiago-Quinonez, D., Rinaldi, C. & Taylor, L. S. Role of Viscosity in Influencing the Glass-Forming Ability of Organic Molecules from the Undercooled Melt State. *Pharmaceutical Research* **29**, 271–284 (July 2011).
14. Koh, C. A., Sloan, E. D., Sum, A. K. & Wu, D. T. Fundamentals and Applications of Gas Hydrates. *Annual Review of Chemical and Biomolecular Engineering* **2**, 237–257 (July 2011).
15. Blaak, R., Auer, S., Frenkel, D. & Löwen, H. Crystal Nucleation of Colloidal Suspensions under Shear. *Physical Review Letters* **93**, 068303 (Aug. 2004).
16. Blaak, R., Auer, S., Frenkel, D. & Löwen, H. Homogeneous nucleation of colloidal melts under the influence of shearing fields. *Journal of Physics: Condensed Matter* **16**, S3873–S3884 (Sept. 2004).
17. Mokshin, A. V. & Barrat, J.-L. Shear induced structural ordering of a model metallic glass. *The Journal of Chemical Physics* **130**, 034502 (Jan. 2009).
18. Graham, R. S. & Olmsted, P. D. Coarse-Grained Simulations of Flow-Induced Nucleation in Semicrystalline Polymers. *Physical Review Letters* **103**, 115702 (Sept. 2009).
19. Radu, M. & Schilling, T. Solvent hydrodynamics speed up crystal nucleation in suspensions of hard spheres. *EPL (Europhysics Letters)* **105**, 26001 (Jan. 2014).
20. Forsyth, C. *et al.* Influence of Controlled Fluid Shear on Nucleation Rates in Glycine Aqueous Solutions. *Crystal Growth & Design* **15**, 94–102 (Nov. 2014).
21. Sharma, M., Madras, G. & Bose, S. Shear induced crystallization in different polymorphic forms of PVDF induced by surface functionalized MWNTs in PVDF/PMMA blends. *Physical Chemistry Chemical Physics* **16**, 16492 (July 2014).
22. Shao, Z. *et al.* Shear-accelerated crystallization in a supercooled atomic liquid. *Physical Review E* **91**, 020301 (Feb. 2015).
23. Stroobants, S. *et al.* Influence of Shear on Protein Crystallization under Constant Shear Conditions. *Crystal Growth & Design* **20**, 1876–1883 (Feb. 2020).
24. Holmqvist, P., Lettinga, M. P., Buitenhuis, J. & Dhont, J. K. G. Crystallization Kinetics of Colloidal Spheres under Stationary Shear Flow. *Langmuir* **21**, 10976–10982 (Nov. 2005).
25. Liu, J. & Rasmuson, Å. C. Influence of Agitation and Fluid Shear on Primary Nucleation in Solution. *Crystal Growth & Design* **13**, 4385–4394 (Sept. 2013).
26. Allen, R. J., Valeriani, C., Tănase-Nicola, S., ten Wolde, P. R. & Frenkel, D. Homogeneous nucleation under shear in a two-dimensional Ising model: Cluster growth, coalescence, and breakup. *The Journal of Chemical Physics* **129**, 134704 (Oct. 2008).
27. Allen, R. J., Valeriani, C. & Tănase-Nicola, S. Nucleation in a Sheared Ising Model: Effects of External Field. *Progress of Theoretical Physics Supplement* **175**, 144–153 (2008).
28. Cerdà, J. J., Sintes, T., Holm, C., Sorensen, C. M. & Chakrabarti, A. Shear effects on crystal nucleation in colloidal suspensions. *Physical Review E* **78**, 031403 (Sept. 2008).
29. Lander, B., Seifert, U. & Speck, T. Crystallization in a sheared colloidal suspension. *The Journal of Chemical Physics* **138**, 224907 (June 2013).
30. Mura, F. & Zaccone, A. Effects of shear flow on phase nucleation and crystallization. *Physical Review E* **93**, 042803 (Apr. 2016).
31. Mokshin, A. V. & Barrat, J.-L. Crystal nucleation and cluster-growth kinetics in a model glass under shear. *Physical Review E* **82**, 021505 (Aug. 2010).
32. Mokshin, A. V., Galimzyanov, B. N. & Barrat, J.-L. Extension of classical nucleation theory for uniformly sheared systems. *Physical Review E* **87**, 062307 (June 2013).
33. Peng, H. L., Herlach, D. M. & Voigtmann, T. Crystal growth in fluid flow: Nonlinear response effects. *Physical Review Materials* **1**, 030401 (Aug. 2017).
34. Luo, S., Wang, J. & Li, Z. Homogeneous Ice Nucleation Under Shear. *The Journal of Physical Chemistry B* **124**, 3701–3708 (Mar. 2020).
35. Goswami, A., Dalal, I. S. & Singh, J. K. Seeding method for ice nucleation under shear. *The Journal of Chemical Physics* **153**, 094502 (Sept. 2020).
36. Goswami, A., Dalal, I. S. & Singh, J. K. Universal Nucleation Behavior of Sheared Systems. *Physical Review Letters* **126**, 195702 (May 2021).

37. Shalf, J. The future of computing beyond Moore's Law. *Philosophical Transactions of the Royal Society A: Mathematical, Physical and Engineering Sciences* **378**, 20190061 (Jan. 2020).
38. Kelton, K. in *Solid State Physics* 75–177 (Elsevier, 1991).
39. Oxtoby, D. W. Homogeneous nucleation: theory and experiment. *Journal of Physics: Condensed Matter* **4**, 7627–7650 (Sept. 1992).
40. Ickes, L., Welti, A., Hoose, C. & Lohmann, U. Classical nucleation theory of homogeneous freezing of water: thermodynamic and kinetic parameters. *Physical Chemistry Chemical Physics* **17**, 5514–5537 (2015).
41. Volmer, M. & Weber, A. Nucleus formation in supersaturated systems. *Z. physik. Chem.* **119**, 277–301 (1926).
42. Becker, R. & Döring, W. Kinetische Behandlung der Keimbildung in übersättigten Dämpfen. *Annalen der Physik* **416**, 719–752 (1935).
43. in. *Selected Works of Yakov Borisovich Zeldovich, Volume I* (ed Sunyaev, R. A.) 120–137 (Princeton University Press, Dec. 1992).
44. Auer, S. & Frenkel, D. Quantitative Prediction of Crystal-Nucleation Rates for Spherical Colloids: A Computational Approach. *Annual Review of Physical Chemistry* **55**, 333–361 (June 2004).
45. Auer, S. & Frenkel, D. in *Advanced Computer Simulation* 149–208 (Springer Berlin Heidelberg, Jan. 2005).
46. Kelton, K. F., Greer, A. L. & Thompson, C. V. Transient nucleation in condensed systems. *The Journal of Chemical Physics* **79**, 6261–6276 (Dec. 1983).
47. Auer, S. & Frenkel, D. Prediction of absolute crystal-nucleation rate in hard-sphere colloids. *Nature* **409**, 1020–1023 (Feb. 2001).
48. Auer, S. & Frenkel, D. Numerical prediction of absolute crystallization rates in hard-sphere colloids. *The Journal of Chemical Physics* **120**, 3015–3029 (Feb. 2004).
49. Pan, A. C. & Chandler, D. Dynamics of Nucleation in the Ising Model†. *The Journal of Physical Chemistry B* **108**, 19681–19686 (Dec. 2004).
50. Nicolis, G. & Nicolis, C. Enhancement of the nucleation of protein crystals by the presence of an intermediate phase: a kinetic model. *Physica A: Statistical Mechanics and its Applications* **323**, 139–154 (May 2003).
51. Pan, W., Kolomeisky, A. B. & Vekilov, P. G. Nucleation of ordered solid phases of proteins via a disordered high-density state: Phenomenological approach. *The Journal of Chemical Physics* **122**, 174905 (May 2005).
52. Talanquer, V. & Oxtoby, D. W. Crystal nucleation in the presence of a metastable critical point. *The Journal of Chemical Physics* **109**, 223–227 (July 1998).
53. Sauter, A. *et al.* On the question of two-step nucleation in protein crystallization. *Faraday Discussions* **179**, 41–58 (2015).
54. Vorontsova, M. A., Maes, D. & Vekilov, P. G. Recent advances in the understanding of two-step nucleation of protein crystals. *Faraday Discussions* **179**, 27–40 (2015).
55. Russo, J. & Tanaka, H. Crystal nucleation as the ordering of multiple order parameters. *The Journal of Chemical Physics* **145**, 211801 (Dec. 2016).
56. Törnquist, M. *et al.* Secondary nucleation in amyloid formation. *Chemical Communications* **54**, 8667–8684 (2018).
57. Kellermeier, M. *et al.* Amino acids form prenucleation clusters: ESI-MS as a fast detection method in comparison to analytical ultracentrifugation. *Faraday Discussions* **159**, 23 (2012).
58. Shore, J. D., Perchak, D. & Shnidman, Y. Simulations of the nucleation of AgBr from solution. *The Journal of Chemical Physics* **113**, 6276–6284 (Oct. 2000).
59. Pontoni, D., Narayanan, T. & Rennie, A. R. in *Trends in Colloid and Interface Science XVI* 227–230 (Springer Berlin Heidelberg, June 2004).
60. Gavezzotti, A. Molecular Aggregation of Acetic Acid in a Carbon Tetrachloride Solution: A Molecular Dynamics Study with a View to Crystal Nucleation. *Chemistry - A European Journal* **5**, 567–576 (Feb. 1999).
61. Salvalaglio, M., Mazzotti, M. & Parrinello, M. Urea homogeneous nucleation mechanism is solvent dependent. *Faraday Discussions* **179**, 291–307 (2015).
62. Erdemir, D. *et al.* Relationship between Self-Association of Glycine Molecules in Supersaturated Solutions and Solid State Outcome. *Physical Review Letters* **99**, 115702 (Sept. 2007).
63. Vehkamäki, H. *Classical Nucleation Theory in Multicomponent Systems* 188 pp. ISBN: 9783540312185 (Springer-Verlag GmbH, Mar. 2006).
64. Parveen, S., Davey, R. J., Dent, G. & Pritchard, R. G. Linking solution chemistry to crystal nucleation: the case of tetrolic acid. *Chemical Communications*, 1531 (2005).
65. Jin, B., Liu, Z. & Tang, R. Recent experimental explorations of non-classical nucleation. *CrystEngComm* **22**, 4057–4073 (2020).

66. Sleutel, M. & Driessche, A. E. S. V. Nucleation of protein crystals – a nanoscopic perspective. *Nanoscale* **10**, 12256–12267 (2018).
67. Erdemir, D., Lee, A. Y. & Myerson, A. S. Nucleation of Crystals from Solution: Classical and Two-Step Models. *Accounts of Chemical Research* **42**, 621–629 (May 2009).
68. Vekilov, P. G. The two-step mechanism of nucleation of crystals in solution. *Nanoscale* **2**, 2346 (2010).
69. Sear, R. P. The non-classical nucleation of crystals: microscopic mechanisms and applications to molecular crystals, ice and calcium carbonate. *International Materials Reviews* **57**, 328–356 (Nov. 2012).
70. Yoreo, J. D. More than one pathway. *Nature Materials* **12**, 284–285 (Mar. 2013).
71. Gebauer, D., Kellermeier, M., Gale, J. D., Bergström, L. & Cölfen, H. Pre-nucleation clusters as solute precursors in crystallisation. *Chem. Soc. Rev.* **43**, 2348–2371 (2014).
72. Zahn, D. Thermodynamics and Kinetics of Prenucleation Clusters, Classical and Non-Classical Nucleation. *ChemPhysChem* **16**, 2069–2075 (Apr. 2015).
73. Zaccaro, J., Matic, J., Myerson, A. S. & Garetz, B. A. Nonphotochemical, Laser-Induced Nucleation of Supersaturated Aqueous Glycine Produces Unexpected  $\gamma$ -Polymorph. *Crystal Growth & Design* **1**, 5–8 (Jan. 2001).
74. Karthika, S., Radhakrishnan, T. K. & Kalaichelvi, P. A Review of Classical and Nonclassical Nucleation Theories. *Crystal Growth & Design* **16**, 6663–6681 (Oct. 2016).
75. Zhang, T. H. & Liu, X. Y. Experimental modelling of single-particle dynamic processes in crystallization by controlled colloidal assembly. *Chem. Soc. Rev.* **43**, 2324–2347 (2014).
76. Xu, J., Reiter, G. & Alamo, R. G. Concepts of Nucleation in Polymer Crystallization. *Crystals* **11**, 304 (Mar. 2021).
77. Abyzov, A. S., Schmelzer, J. W. P., Fokin, V. M. & Zanotto, E. D. Crystallization of Supercooled Liquids: Self-Consistency Correction of the Steady-State Nucleation Rate. *Entropy* **22**, 558 (May 2020).
78. Espinosa, J. R., Sanz, E., Valeriani, C. & Vega, C. Homogeneous ice nucleation evaluated for several water models. *The Journal of Chemical Physics* **141**, 18C529 (Nov. 2014).
79. Espinosa, J. R., Vega, C., Valeriani, C. & Sanz, E. Seeding approach to crystal nucleation. *The Journal of Chemical Physics* **144**, 034501 (Jan. 2016).
80. Lutsko, J. F. Systematically extending classical nucleation theory. *New Journal of Physics* **20**, 103015 (Oct. 2018).
81. Bai, X.-M. & Li, M. Test of classical nucleation theory via molecular-dynamics simulation. *The Journal of Chemical Physics* **122**, 224510 (June 2005).
82. Knott, B. C., Molinero, V., Doherty, M. F. & Peters, B. Homogeneous Nucleation of Methane Hydrates: Unrealistic under Realistic Conditions. *Journal of the American Chemical Society* **134**, 19544–19547 (Nov. 2012).
83. Sanz, E. *et al.* Homogeneous Ice Nucleation at Moderate Supercooling from Molecular Simulation. *Journal of the American Chemical Society* **135**, 15008–15017 (Sept. 2013).
84. Prestipino, S., Laio, A. & Tosatti, E. Systematic Improvement of Classical Nucleation Theory. *Physical Review Letters* **108**, 225701 (May 2012).
85. Haji-Akbari, A. & Debenedetti, P. G. Direct calculation of ice homogeneous nucleation rate for a molecular model of water. *Proceedings of the National Academy of Sciences* **112**, 10582–10588 (Aug. 2015).
86. Jiang, H., Haji-Akbari, A., Debenedetti, P. G. & Panagiotopoulos, A. Z. Forward flux sampling calculation of homogeneous nucleation rates from aqueous NaCl solutions. *The Journal of Chemical Physics* **148**, 044505 (Jan. 2018).
87. Li, T., Donadio, D., Russo, G. & Galli, G. Homogeneous ice nucleation from supercooled water. *Physical Chemistry Chemical Physics* **13**, 19807 (2011).
88. Russo, J., Romano, F. & Tanaka, H. New metastable form of ice and its role in the homogeneous crystallization of water. *Nature Materials* **13**, 733–739 (May 2014).
89. Pruppacher, H. R. A New Look at Homogeneous Ice Nucleation in Supercooled Water Drops. *Journal of the Atmospheric Sciences* **52**, 1924–1933 (June 1995).
90. Stöckel, P., Weidinger, I. M., Baumgärtel, H. & Leisner, T. Rates of Homogeneous Ice Nucleation in Levitated H<sub>2</sub>O and D<sub>2</sub>O Droplets†. *The Journal of Physical Chemistry A* **109**, 2540–2546 (Mar. 2005).
91. Murray, B. J. *et al.* Kinetics of the homogeneous freezing of water. *Physical Chemistry Chemical Physics* **12**, 10380 (2010).
92. Atkinson, J. D., Murray, B. J. & O’Sullivan, D. Rate of Homogenous Nucleation of Ice in Supercooled Water. *The Journal of Physical Chemistry A* **120**, 6513–6520 (Aug. 2016).

93. Bai, X.-M. & Li, M. Calculation of solid-liquid interfacial free energy: A classical nucleation theory based approach. *The Journal of Chemical Physics* **124**, 124707 (Mar. 2006).
94. Pereyra, R. G., Szleifer, I. & Carignano, M. A. Temperature dependence of ice critical nucleus size. *The Journal of Chemical Physics* **135**, 034508 (July 2011).
95. Espinosa, J. R., Vega, C., Valeriani, C. & Sanz, E. The crystal-fluid interfacial free energy and nucleation rate of NaCl from different simulation methods. *The Journal of Chemical Physics* **142**, 194709 (May 2015).
96. Zimmermann, N. E. R., Vorselaars, B., Quigley, D. & Peters, B. Nucleation of NaCl from Aqueous Solution: Critical Sizes, Ion-Attachment Kinetics, and Rates. *Journal of the American Chemical Society* **137**, 13352–13361 (Oct. 2015).
97. Zimmermann, N. E. R. *et al.* NaCl nucleation from brine in seeded simulations: Sources of uncertainty in rate estimates. *The Journal of Chemical Physics* **148**, 222838 (June 2018).
98. Richard, D. & Speck, T. Crystallization of hard spheres revisited. II. Thermodynamic modeling, nucleation work, and the surface of tension. *The Journal of Chemical Physics* **148**, 224102 (June 2018).
99. Evans, D. J. & Morriss, G. P. Nonlinear-response theory for steady planar Couette flow. *Physical Review A* **30**, 1528–1530 (Sept. 1984).
100. Lees, A. W. & Edwards, S. F. The computer study of transport processes under extreme conditions. *Journal of Physics C: Solid State Physics* **5**, 1921–1928 (Aug. 1972).
101. Daivis, P. J. & Todd, B. D. A simple, direct derivation and proof of the validity of the SLLOD equations of motion for generalized homogeneous flows. *The Journal of Chemical Physics* **124**, 194103 (May 2006).
102. Brandel, C. & ter Horst, J. H. Measuring induction times and crystal nucleation rates. *Faraday Discussions* **179**, 199–214 (2015).
103. Fitzner, M., Sosso, G. C., Cox, S. J. & Michaelides, A. The Many Faces of Heterogeneous Ice Nucleation: Interplay Between Surface Morphology and Hydrophobicity. *Journal of the American Chemical Society* **137**, 13658–13669 (Oct. 2015).
104. Resnick, S. I. *Adventures in Stochastic Processes* 640 pp. ISBN: 1461267382 (Birkhäuser Boston, Dec. 2013).
105. Wedekind, J., Strey, R. & Reguera, D. New method to analyze simulations of activated processes. *The Journal of Chemical Physics* **126**, 134103 (Apr. 2007).
106. Hänggi, P., Talkner, P. & Borkovec, M. Reaction-rate theory: fifty years after Kramers. *Reviews of Modern Physics* **62**, 251–341 (Apr. 1990).
107. Lundrigan, S. E. M. & Saika-Voivod, I. Test of classical nucleation theory and mean first-passage time formalism on crystallization in the Lennard-Jones liquid. *The Journal of Chemical Physics* **131**, 104503 (2009).
108. Allen, R. J., Frenkel, D. & ten Wolde, P. R. Simulating rare events in equilibrium or nonequilibrium stochastic systems. *The Journal of Chemical Physics* **124**, 024102 (Jan. 2006).
109. Allen, R. J., Warren, P. B. & ten Wolde, P. R. Sampling Rare Switching Events in Biochemical Networks. *Physical Review Letters* **94**, 018104 (Jan. 2005).
110. Dellago, C., Bolhuis, P. G., Csajka, F. S. & Chandler, D. Transition path sampling and the calculation of rate constants. *The Journal of Chemical Physics* **108**, 1964–1977 (Feb. 1998).
111. Dellago, C., Bolhuis, P. G. & Chandler, D. On the calculation of reaction rate constants in the transition path ensemble. *The Journal of Chemical Physics* **110**, 6617–6625 (Apr. 1999).
112. Bolhuis, P. G., Chandler, D., Dellago, C. & Geissler, P. L. TRANSITIONPATHSAMPLING: Throwing Ropes Over Rough Mountain Passes, in the Dark. *Annual Review of Physical Chemistry* **53**, 291–318 (Oct. 2002).
113. Van Erp, T. S., Moroni, D. & Bolhuis, P. G. A novel path sampling method for the calculation of rate constants. *The Journal of Chemical Physics* **118**, 7762–7774 (May 2003).
114. Van Erp, T. S. & Bolhuis, P. G. Elaborating transition interface sampling methods. *Journal of Computational Physics* **205**, 157–181 (May 2005).
115. Faradjian, A. K. & Elber, R. Computing time scales from reaction coordinates by milestoning. *The Journal of Chemical Physics* **120**, 10880–10889 (June 2004).
116. West, A. M. A., Elber, R. & Shalloway, D. Extending molecular dynamics time scales with milestoning: Example of complex kinetics in a solvated peptide. *The Journal of Chemical Physics* **126**, 145104 (Apr. 2007).
117. Allen, R. J., Valeriani, C. & ten Wolde, P. R. Forward flux sampling for rare event simulations. *Journal of Physics: Condensed Matter* **21**, 463102 (Oct. 2009).
118. Hussain, S. & Haji-Akbari, A. Studying rare events using forward-flux sampling: Recent breakthroughs and future outlook. *The Journal of Chemical Physics* **152**, 060901 (Feb. 2020).
119. Kratzer, K., Berryman, J. T., Taudt, A., Zeman, J. & Arnold, A. The Flexible Rare Event Sampling Harness System (FRESHS). *Computer Physics Communications* **185**, 1875–1885 (July 2014).

120. Kramers, H. Brownian motion in a field of force and the diffusion model of chemical reactions. *Physica* **7**, 284–304 (Apr. 1940).
121. Zwanzig, R. *Nonequilibrium statistical mechanics* (Oxford University Press, 2001).
122. Richard, D. & Speck, T. Classical nucleation theory for the crystallization kinetics in sheared liquids. *Physical Review E* **99**, 062801 (June 2019).
123. Siqueira, I., Rebouças, R. & Carvalho, M. Migration and alignment in the flow of elongated particle suspensions through a converging-diverging channel. *Journal of Non-Newtonian Fluid Mechanics* **243**, 56–63 (May 2017).
124. Chandran, K., Dalal, I. S., Tatsumi, K. & Muralidhar, K. Numerical simulation of blood flow modeled as a fluid-particulate mixture. *Journal of Non-Newtonian Fluid Mechanics* **285**, 104383 (Nov. 2020).
125. Cao, P. *et al.* Mechanical properties of bi- and poly-crystalline ice. *AIP Advances* **8**, 125108 (Dec. 2018).
126. Yang, F. Homogeneous nucleation in a Poiseuille flow. *Physical Chemistry Chemical Physics* **23**, 3974–3982 (2021).
127. Richard, D. & Speck, T. The role of shear in crystallization kinetics: From suppression to enhancement. *Scientific Reports* **5**, 1–7 (Sept. 2015).
128. Pettersson, L. G. M., Henchman, R. H. & Nilsson, A. Water—The Most Anomalous Liquid. *Chemical Reviews* **116**, 7459–7462 (July 2016).
129. Sutherland, W. LXXV. A dynamical theory of diffusion for non-electrolytes and the molecular mass of albumin. *The London, Edinburgh, and Dublin Philosophical Magazine and Journal of Science* **9**, 781–785 (June 1905).
130. Hynes, J. T. Statistical Mechanics of Molecular Motion in Dense Fluids. *Annual Review of Physical Chemistry* **28**, 301–321 (Oct. 1977).
131. Alder, B. J. & Wainwright, T. E. Phase Transition for a Hard Sphere System. *The Journal of Chemical Physics* **27**, 1208–1209 (Nov. 1957).
132. Alder, B. J., Hoover, W. G. & Young, D. A. Studies in Molecular Dynamics. V. High-Density Equation of State and Entropy for Hard Disks and Spheres. *The Journal of Chemical Physics* **49**, 3688–3696 (Oct. 1968).
133. Gasser, U. Real-Space Imaging of Nucleation and Growth in Colloidal Crystallization. *Science* **292**, 258–262 (Apr. 2001).
134. Dullens, R. P. A., Aarts, D. G. A. L. & Kegels, W. K. Dynamic Broadening of the Crystal-Fluid Interface of Colloidal Hard Spheres. *Physical Review Letters* **97**, 228301 (Nov. 2006).
135. Vega, C. & Noya, E. G. Revisiting the Frenkel-Ladd method to compute the free energy of solids: The Einstein molecule approach. *The Journal of Chemical Physics* **127**, 154113 (Oct. 2007).
136. Pusey, P. N. *et al.* Hard spheres: crystallization and glass formation. *Philosophical Transactions of the Royal Society A: Mathematical, Physical and Engineering Sciences* **367**, 4993–5011 (Dec. 2009).
137. Zaccarelli, E. *et al.* Crystallization of Hard-Sphere Glasses. *Physical Review Letters* **103**, 135704 (Sept. 2009).
138. Valeriani, C. *et al.* Crystallization and aging in hard-sphere glasses. *Journal of Physics: Condensed Matter* **23**, 194117 (Apr. 2011).
139. Valeriani, C. *et al.* From compact to fractal crystalline clusters in concentrated systems of monodisperse hard spheres. *Soft Matter* **8**, 4960 (2012).
140. Vermant, J. & Solomon, M. J. Flow-induced structure in colloidal suspensions. *Journal of Physics: Condensed Matter* **17**, R187–R216 (Jan. 2005).
141. Galimzyanov, B. N. & Mokshin, A. V. Morphology of critically sized crystalline nuclei at shear-induced crystal nucleation in amorphous solid. *Journal of Rheology* **62**, 265–275 (Jan. 2018).
142. Binsbergen, F. L. Orientation-induced Nucleation in Polymer Crystallization. *Nature* **211**, 516–517 (July 1966).
143. Kimata, S. *et al.* Molecular Basis of the Shish-Kebab Morphology in Polymer Crystallization. *Science* **316**, 1014–1017 (May 2007).
144. Mykhaylyk, O. O. *et al.* The Specific Work of Flow as a Criterion for Orientation in Polymer Crystallization. *Macromolecules* **41**, 1901–1904 (Mar. 2008).
145. Read, D. J., McIlroy, C., Das, C., Harlen, O. G. & Graham, R. S. PolySTRAND Model of Flow-Induced Nucleation in Polymers. *Physical Review Letters* **124**, 147802 (Apr. 2020).
146. Hsiao, B. S., Yang, L., Somani, R. H., Avila-Orta, C. A. & Zhu, L. Unexpected Shish-Kebab Structure in a Sheared Polyethylene Melt. *Physical Review Letters* **94**, 117802 (Mar. 2005).
147. Dargazany, R., Khiêm, V. N., Poshtan, E. A. & Itskov, M. Constitutive modeling of strain-induced crystallization in filled rubbers. *Physical Review E* **89**, 022604 (Feb. 2014).
148. De Koning, M. Crystal imperfections in ice Ih. *The Journal of Chemical Physics* **153**, 110902 (Sept. 2020).

149. Pingua, N. & Apte, P. A. Topological Identification Criteria, Stability, and Relevance of Pentagonal Nanochannels in Amorphous Ice. *The Journal of Physical Chemistry B* **123**, 10301–10310 (Nov. 2019).
150. Johnston, J. C. & Molinero, V. Crystallization, Melting, and Structure of Water Nanoparticles at Atmospherically Relevant Temperatures. *Journal of the American Chemical Society* **134**, 6650–6659 (Apr. 2012).
151. Goswami, A. & Singh, J. K. A hybrid topological and shape-matching approach for structure analysis. *The Journal of Chemical Physics* **154**, 154502 (Apr. 2021).
152. Kumaraswamy, G., Kornfield, J. A., Yeh, F. & Hsiao, B. S. Shear-Enhanced Crystallization in Isotactic Polypropylene. 3. Evidence for a Kinetic Pathway to Nucleation. *Macromolecules* **35**, 1762–1769 (Feb. 2002).
153. *Nucleation Theory and Applications* (ed Schmelzer, J. W. P.) (Wiley, Jan. 2005).
154. Duff, N. & Lacks, D. J. Shear-induced crystallization in jammed systems. *Physical Review E* **75**, 031501 (Mar. 2007).
155. Mokshin, A. V. & Barrat, J.-L. Shear-induced crystallization of an amorphous system. *Physical Review E* **77**, 021505 (Feb. 2008).
156. Kerrache, A., Mousseau, N. & Lewis, L. J. Crystallization of amorphous silicon induced by mechanical shear deformations. *Physical Review B* **84**, 014110 (July 2011).
157. Samon, J. M. *et al.* Structure Development during the Melt Spinning of Polyethylene and Poly(vinylidene fluoride) Fibers by in Situ Synchrotron Small- and Wide-Angle X-ray Scattering Techniques. *Macromolecules* **32**, 8121–8132 (Nov. 1999).
158. Doufas, A. K., McHugh, A. J. & Miller, C. Simulation of melt spinning including flow-induced crystallization. *Journal of Non-Newtonian Fluid Mechanics* **92**, 27–66 (Aug. 2000).
159. Zheng, G.-Q. *et al.* Flow-induced fiber orientation in gas-assisted injection molded part. *Materials Letters* **61**, 3436–3439 (June 2007).
160. Xu, Z.-b., Su, L.-y., Wang, P.-f. & Peng, M. Effect of oscillatory shear on the mechanical properties and crystalline morphology of linear low density polyethylene. *Chinese Journal of Polymer Science* **33**, 1114–1124 (June 2015).
161. Graham, R. S. & Olmsted, P. D. Kinetic Monte Carlo simulations of flow-induced nucleation in polymer melts. *Faraday Discuss.* **144**, 71–92 (2010).
162. Wool, R. P. Polymer entanglements. *Macromolecules* **26**, 1564–1569 (Mar. 1993).
163. McLeish, T. C. B. Tube theory of entangled polymer dynamics. *Advances in Physics* **51**, 1379–1527 (Sept. 2002).
164. Graham, R. S. Molecular modelling of flow-induced crystallisation in polymers. *Journal of Engineering Mathematics* **71**, 237–251 (Oct. 2010).
165. Graham, R. S. Modelling flow-induced crystallisation in polymers. *Chem. Commun.* **50**, 3531–3545 (2014).
166. Wang, Z., Ma, Z. & Li, L. Flow-Induced Crystallization of Polymers: Molecular and Thermodynamic Considerations. *Macromolecules* **49**, 1505–1517 (Feb. 2016).
167. Cui, K. *et al.* Multiscale and Multistep Ordering of Flow-Induced Nucleation of Polymers. *Chemical Reviews* **118**, 1840–1886 (Jan. 2018).
168. Graham, R. S. Understanding flow-induced crystallization in polymers: A perspective on the role of molecular simulations. *Journal of Rheology* **63**, 203–214 (Jan. 2019).
169. Jabbarzadeh, A. & Tanner, R. Crystallization of alkanes under quiescent and shearing conditions. *Journal of Non-Newtonian Fluid Mechanics* **160**, 11–21 (July 2009).
170. Balzano, L., Kukalyekar, N., Rastogi, S., Peters, G. W. M. & Chadwick, J. C. Crystallization and Dissolution of Flow-Induced Precursors. *Physical Review Letters* **100**, 048302 (Feb. 2008).
171. Anwar, M., Berryman, J. T. & Schilling, T. Crystal nucleation mechanism in melts of short polymer chains under quiescent conditions and under shear flow. *The Journal of Chemical Physics* **141**, 124910 (Sept. 2014).
172. Coppola, S., Balzano, L., Gioffredi, E., Maffettone, P. L. & Grizzuti, N. Effects of the degree of undercooling on flow induced crystallization in polymer melts. *Polymer* **45**, 3249–3256 (May 2004).
173. Anwar, M. & Graham, R. S. Molecular dynamics simulations of crystal nucleation in entangled polymer melts under start-up shear conditions. *The Journal of Chemical Physics* **150**, 084905 (Feb. 2019).
174. Graham, R. S., Likhthman, A. E., McLeish, T. C. B. & Milner, S. T. Microscopic theory of linear, entangled polymer chains under rapid deformation including chain stretch and convective constraint release. *Journal of Rheology* **47**, 1171–1200 (Sept. 2003).
175. Huang, L. & Makarov, D. E. The rate constant of polymer reversal inside a pore. *The Journal of Chemical Physics* **128**, 114903 (Mar. 2008).
176. Hernández-Ortiz, J. P., Chopra, M., Geier, S. & de Pablo, J. J. Hydrodynamic effects on the translocation rate of a polymer through a pore. *The Journal of Chemical Physics* **131**, 044904 (July 2009).

177. Růžička, Š., Quigley, D. & Allen, M. P. Folding kinetics of a polymer. *Phys. Chem. Chem. Phys.* **14**, 6044–6053 (2012).
178. Cao, J., Zhu, J., Wang, Z. & Likhtman, A. E. Large deviations of Rouse polymer chain: First passage problem. *The Journal of Chemical Physics* **143**, 204105 (Nov. 2015).
179. Zhu, J., Likhtman, A. E. & Wang, Z. Arm retraction dynamics of entangled star polymers: A forward flux sampling method study. *The Journal of Chemical Physics* **147**, 044907 (July 2017).
180. Rezvantalab, H. & Larson, R. G. Bridging Dynamics of Telechelic Polymers between Solid Surfaces. *Macromolecules* **51**, 2125–2137 (Mar. 2018).
181. Bauerecker, S., Ulbig, P., Buch, V., Vrbka, L. & Jungwirth, P. Monitoring Ice Nucleation in Pure and Salty Water via High-Speed Imaging and Computer Simulations. *The Journal of Physical Chemistry C* **112**, 7631–7636 (May 2008).
182. Manka, A. *et al.* Freezing water in no-man's land. *Physical Chemistry Chemical Physics* **14**, 4505 (2012).
183. Riechers, B., Wittbracht, F., Hütten, A. & Koop, T. The homogeneous ice nucleation rate of water droplets produced in a microfluidic device and the role of temperature uncertainty. *Physical Chemistry Chemical Physics* **15**, 5873 (2013).
184. Sellberg, J. A. *et al.* Ultrafast X-ray probing of water structure below the homogeneous ice nucleation temperature. *Nature* **510**, 381–384 (June 2014).
185. Laksmono, H. *et al.* Anomalous Behavior of the Homogeneous Ice Nucleation Rate in “No-Man's Land”. *The Journal of Physical Chemistry Letters* **6**, 2826–2832 (July 2015).
186. Mishima, O. & Stanley, H. E. The relationship between liquid, supercooled and glassy water. *Nature* **396**, 329–335 (Nov. 1998).
187. Xu, Y., Petrik, N. G., Smith, R. S., Kay, B. D. & Kimmel, G. A. Growth rate of crystalline ice and the diffusivity of supercooled water from 126 to 262 K. *Proceedings of the National Academy of Sciences* **113**, 14921–14925 (Dec. 2016).
188. Handle, P. H., Loerting, T. & Sciortino, F. Supercooled and glassy water: Metastable liquid(s), amorphous solid(s), and a no-man's land. *Proceedings of the National Academy of Sciences* **114**, 13336–13344 (Nov. 2017).
189. Kim, K. H. *et al.* Maxima in the thermodynamic response and correlation functions of deeply supercooled water. *Science* **358**, 1589–1593 (Dec. 2017).
190. Ni, Y., Hestand, N. J. & Skinner, J. L. Communication: Diffusion constant in supercooled water as the Widom line is crossed in no man's land. *The Journal of Chemical Physics* **148**, 191102 (May 2018).
191. Saito, S. & Bagchi, B. Thermodynamic picture of vitrification of water through complex specific heat and entropy: A journey through “no man's land”. *The Journal of Chemical Physics* **150**, 054502 (Feb. 2019).
192. Dixit, N. M., Kulkarni, A. M. & Zukoski, C. F. Comparison of experimental estimates and model predictions of protein crystal nucleation rates. *Colloids and Surfaces A: Physicochemical and Engineering Aspects* **190**, 47–60 (Sept. 2001).
193. Blow, K. E., Quigley, D. & Sosso, G. C. The Seven Deadly Sins: when computing crystal nucleation rates, the devil is in the details. arXiv: 2104.13104 [cond-mat.mtrl-sci] (Apr. 2021).
194. Panine, P., Narayanan, T., Vermant, J. & Mewis, J. Structure and rheology during shear-induced crystallization of a latex suspension. *Physical Review E* **66**, 022401 (Aug. 2002).
195. Liu, J., Svård, M. & Rasmuson, Å. C. Influence of Agitation and Fluid Shear on Nucleation of m-Hydroxybenzoic Acid Polymorphs. *Crystal Growth & Design* **14**, 5521–5531 (Oct. 2014).
196. Southern, J. H. & Porter, R. S. The properties of polyethylene crystallized under the orientation and pressure effects of a pressure capillary viscometer. *Journal of Applied Polymer Science* **14**, 2305–2317 (Sept. 1970).
197. Southern, J. H. & Porter, R. S. Polyethylene crystallized under the orientation and pressure of a pressure capillary viscometer. Part I. *Journal of Macromolecular Science, Part B* **4**, 541–555 (Sept. 1970).
198. Crystal, R. G. & Southern, J. H. Morphology of polyethylene crystallized under the simultaneous influence of pressure and orientation in a capillary viscometer. *Journal of Polymer Science Part A-2: Polymer Physics* **9**, 1641–1655 (Sept. 1971).
199. Southern, J. H., Porter, R. S. & Bair, H. E. Melting behavior of polyethylene crystallized in a pressure capillary viscometer. *Journal of Polymer Science Part A-2: Polymer Physics* **10**, 1135–1143 (June 1972).
200. Haas, T. W. & Maxwell, B. Effects of shear stress on the crystallization of linear polyethylene and polybutene-1. *Polymer Engineering and Science* **9**, 225–241 (July 1969).
201. Janeschitz-Kriegl, H. & Eder, G. Basic Concepts of Structure Formation During Processing of Thermoplastic Materials. *Journal of Macromolecular Science: Part A - Chemistry* **27**, 1733–1756 (Nov. 1990).

202. Kumaraswamy, G., Verma, R. K. & Kornfield, J. A. Novel flow apparatus for investigating shear-enhanced crystallization and structure development in semicrystalline polymers. *Review of Scientific Instruments* **70**, 2097–2104 (Apr. 1999).
203. Geng, Y. *et al.* Shear-Induced Nucleation and Growth of Long Helices in Supercooled Isotactic Polypropylene. *Macromolecules* **42**, 4751–4757 (May 2009).
204. Kornfield, J. A., Kumaraswamy, G. & Issaian, A. M. Recent Advances in Understanding Flow Effects on Polymer Crystallization. *Industrial & Engineering Chemistry Research* **41**, 6383–6392 (Dec. 2002).
205. Bekard, I. B., Asimakis, P., Bertolini, J. & Dunstan, D. E. The effects of shear flow on protein structure and function. *Biopolymers*, n/a–n/a (2011).
206. Jung, T., Kim, W.-S. & Choi, C. K. Effect of Nonstoichiometry on Reaction Crystallization of Calcium Carbonate in a Couette-Taylor Reactor. *Crystal Growth & Design* **4**, 491–495 (May 2004).
207. Luo, S., Li, C., Li, F., Wang, J. & Li, Z. Ice Crystallization in Shear Flows. *The Journal of Physical Chemistry C* **123**, 21042–21049 (Aug. 2019).
208. Pedevilla, P., Fitzner, M., Sosso, G. C. & Michaelides, A. Heterogeneous seeded molecular dynamics as a tool to probe the ice nucleating ability of crystalline surfaces. *The Journal of Chemical Physics* **149**, 072327 (Aug. 2018).
209. Fitzner, M., Pedevilla, P. & Michaelides, A. Predicting heterogeneous ice nucleation with a data-driven approach. *Nature Communications* **11**, 1–9 (Sept. 2020).